Constitutive modeling of rate and temperature dependent strain hardening in polycarbonate

Krop, S.

Award date:
2011

Constitutive modeling of rate and temperature dependent strain hardening in polycarbonate

S. Krop

Master thesis, MT 11.xx

Eindhoven University of Technology
Department of Mechanical Engineering
Section Polymer Technology

prof. dr. ir. H.E.H. Meijer
dr. ir. L.E. Govaert
dr. ir. J.A.W. van Dommelen
ir. D.J.A. Senden (advisor)

Eindhoven, August 22, 2011

Contents

1 Introduction 1

2 Background 4

3 Phenomenology 8

4 Constitutive modeling 13
- 4.1 Kinematics . . . 13
- 4.2 Stress calculation . . . 14
- 4.3 Strain hardening: elastic contribution . . . 16
- 4.4 Strain hardening: viscous contribution . . . 18

5 Simulation results 20
- 5.1 Model characterization . . . 20
- 5.2 Simulation results . . . 24

6 Discussion 27

7 Conclusion 31

Bibliography 31

A Parameters EGP model 34

B 1-D stress from EGP model 36

C Edwards-Vilgis theory 38

Abstract

In most established constitutive models describing glassy polymers, strain hardening is modeled as a rubber-elastic response of the entanglement network. This approach works well when describing the mechanical response in experiments where the deformation increases monotonically, but it fails when the loading direction is reversed. This implies that the response of oriented glassy polymers cannot be captured in this manner. Recently it was proposed that this issue can be resolved by modeling strain hardening with a combined viscous and elastic contribution. Other indications that a rubber-elastic strain hardening model is inadequate, is that it fails to describe the experimentally observed effects of strain rate and temperature. This study aims to characterize the proposed viscous contribution of strain hardening by evaluating the intrinsic behavior of polycarbonate (PC) over a large range of strain rates and temperatures. From this, it is concluded that the deformation dependence manifests itself in the rate constant and the activation energy, both parameters in the Eyring flow stress. With simulations using the Eindhoven Glassy Polymer (EGP) model it is demonstrated that this approach quantitatively captures the large strain mechanical response of PC over a vast range of strain rates and temperatures. Moreover, the adapted model provides quantitative predictions of the yield kinetics of oriented polymers.

Chapter 1

Introduction

The post-yield response of glassy polymers displays two characteristic phenomena: (i) strain softening, the initial decrease of true stress with increasing strain, which is related to a structural evolution that reduces the material's resistance to plastic deformation, and (ii) strain hardening, characterized by the increase in stress at high strain, which originates from the network of entangled polymer chains that orients with deformation. The macroscopic behavior of a glassy polymer is strongly determined by the interplay between these two effects. On the one hand, strain softening tends to destabilize the deformation, which may lead to the formation of localized plastic deformation zones, especially in the vicinity of stress concentrations. The evolution of these plastic zones, on the other hand, strongly depends on the stabilizing effect of strain hardening. A relatively strong strain hardening effect stabilizes the deformation zones, which enables them to expand in a controlled fashion, leading to macroscopically ductile behavior such as shear band formation and necking. With insufficient strain hardening, in contrast, the material tends to form crazes. These are extremely localized zones of plastic deformation, which may lead to the formation of cracks, resulting in macroscopically brittle behavior [3, 20]. Therefore, it is clear that a better understanding of the origin of strain hardening is an essential aspect in the design of polymer systems [18].

An important observation in this field was that, when heated above the glass transition temperature T_g, the plastic deformation of a glassy polymer is almost fully recovered [14]. This suggests that the entanglement network remains largely intact during plastic deformation, inspiring Haward and Thackray [15] to propose a 1-D constitutive relation in which the postyield stress response is decomposed in two components. A viscous component, which is referred to as the flow stress, describes the intermolecular interactions on a segmental scale. In parallel, an elastic component is used to model the entropic-elastic response of the entangled molecular network. This concept is employed in several 3-D constitutive models, such as the Oxford Glass-Rubber (OGR) model [6], the Boyce-Parks-Argon (BPA) model [4] and the Eindhoven Glassy Polymer (EGP) model [13, 16]. In all of these models, the experimentally observed strain hardening is modeled using a nonlinear rubber-elastic contribution originating from hyperelasticity theory. Generally, these can be expressed as:

$$\sigma = NkT \cdot f(\lambda), \tag{1.1}$$

where N describes the network density, i.e. the number of chains per unit volume in the network, k is Boltzmann's constant, T the temperature and $f(\lambda)$ a measure of the strain. These models prove useful from a phenomenological point of view, by describing the constitutive behavior below T_g for constant temperature and strain rate, but all exhibit important inconsistencies with the underlying polymer physics and experimental observations. Firstly, the apparent network density required for fitting the experimental results is orders of magnitudes larger than the entanglement density evaluated from the melt [11]. Secondly, strain hardening is sensitive to the applied strain

rate [28], which is inconsistent with the rubber-elastic modeling of the phenomenon. And thirdly, strain hardening decreases with increasing temperature [12], which is inconsistent with entropic elasticity. Clearly these are major flaws and it is therefore eminent that improvements are needed to solve these problems.

Considering the inconsistencies in these kind of models, there is a growing recognition that they are inadequate in describing large deformations in polymer glasses over a wide range of strain rates and temperatures. One possible route to improve this is the introduction of a viscous contribution to strain hardening, as was explored by Wendlandt *et al.* [28], who presented experimental evidence of a rate dependence in the strain hardening for a number of polymers. Their method of introducing a deformation dependence in the Eyring flow stress via the activation volume proved successful in describing uniaxial compression experiments at various strain rates. Another indication of a viscous contribution to train hardening was provided by Senden *et al.* [24], who investigated the Bauschinger effect in oriented polymers. This Bauschinger effect was observed when comparing tensile tests with compressive tests on samples with the same level of orientation: in tension the yield stress increased with preorientation, while in compressionit remained the same. With constitutive models like the ones mentioned before (OGR, BPA, EGP), this Bauschinger effect can not be described. By means of a *gedankenexperiment* it was rationalized that this could be solved by modeling strain hardening with both a viscous contribution and an elastic contribution. Furthermore, it was shown that for the resulting deformation dependence in the flow stress, basically two modeling choices are at hand. The flow stress is described with an Eyring type relation [10], which

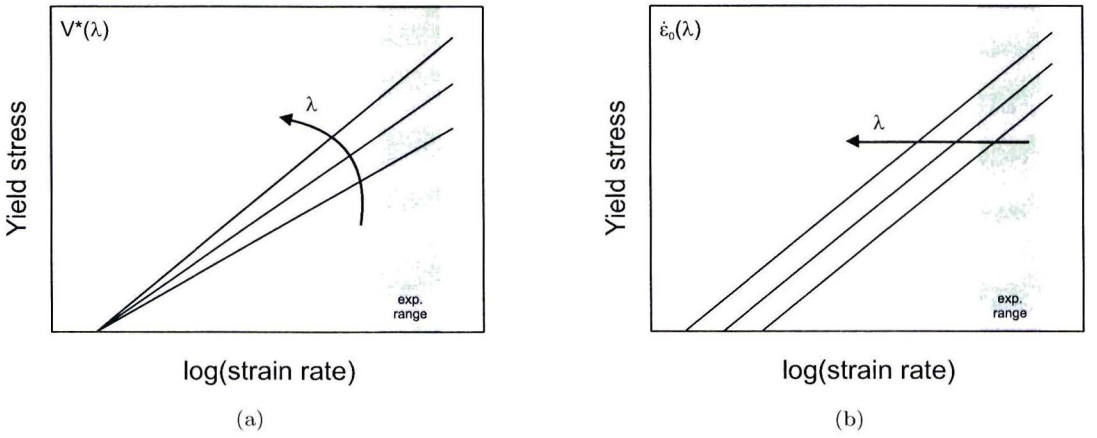

Figure 1.1: Schematic illustration of the effect of deformation on the yield kinetics in case of a deformation dependent (a) activation volume, and (b) rate constant.

is characterized by two parameters. How the material is affected by strain rate is captured by the activation volume V^* (i.e. yield kinetics), while a rate constant $\dot{\varepsilon}_0$ determines the initial state of the material. This implies that a deformation dependence in the activation volume (Figure 1.1a) can be interpreted as a gradual change of the yield kinetics, i.e. the slope when plotting yield stress as a function of the logarithm of the strain rate, with increasing deformation; modeling it in the rate constant (Figure 1.1b) leaves the yield kinetics (i.e. the slope) unaffected, but instead shifts the process to lower strain rates.

Over the past years, the Eindhoven Glassy Polymer (EGP) model has become well-established for accurately describing and predicting the mechanical response of amorphous polymers in transient loading. However, it also exhibits the aforementioned major flaws that are associated with modeling strain hardening as a purely rubber-elastic phenomenon. The goal of this study is to improve its performance by investigating the possibilities of a viscous contribution to strain hardening,

making use of the relevant experimental observations that have been reported in literature, while preserving its qualities. Polycarbonate is used as a model material. After a brief introduction of the mechanical behavior of polymers and its relation with temperature and strain rate (Chapter 2), the phenomenology of deformation dependence of flow stress is investigated (Chapter 3). The EGP model in its present form and the implications of a viscous contribution are discussed in Chapter 4. Finally, in Chapter 5 the modifications are quantified and compared to experimental data using numerical simulations.

Chapter 2

Background

Intrinsic behavior

The intrinsic deformation behavior, defined as the true stress-strain response during homogeneous deformation, for polycarbonate is shown in Figure 2.1, measured in uniaxial compression at different strain rates and temperatures. At small strains a viscoelastic region is observed, which is initially linear elastic but becomes progressively nonlinear with increased loading. At the yield point, which is the first maximum in the curve, the stress is high enough to overcome intermolecular forces, allowing large scale segmental motion of the polymer chains. The subsequent stress decrease with increasing strain is called strain softening. This decrease in stress tends to destabilize the deformation, which, in other loading geometries such as tension, may lead to strain localization. After a minimum in the stress (lower yield point) the mechanical response is dominated by strain hardening, causing an upswing in stress that stabilizes the deformation. As mentioned in the introduction, strain hardening originates from the stretching of the entanglement network. Polycarbonate exhibits limited strain softening, which can easily be stabilized by the strong strain hardening, resulting in a generally tough response.

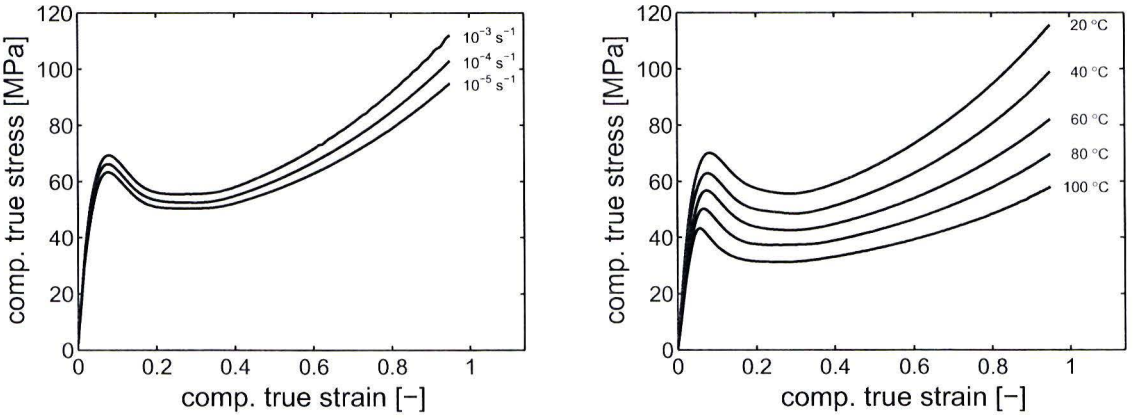

(a) $T = 23°C$ (b) $\dot{\varepsilon} = 10^{-3}s^{-1}$

Figure 2.1: The intrinsic deformation behavior of polycarbonate, measured in uniaxial compression (a) at different true strain rates and (b) at different temperatures (data taken from [9]).

Effect of strain rate and temperature

Where the intrinsic behavior gives insight in the general stress-strain response, the strain rate and temperature dependence can be studied in more detail by considering the yield kinetics. This is

demonstrated in Figure 2.2, where the upper and lower yield points of the curves in Figure 2.1 are plotted as both a function of strain rate and of temperature. From Figure 2.2a it is clear that both the (upper) yield stress and the lower yield stress linearly depend on the logarithm of the applied strain rate. Moreover, the slopes are equal, as is demonstrated by the yield drop, i.e. the difference between upper and lower yield, which is constant. This indicates that both are governed by the same kinetics. In Figure 2.2b it is demonstrated that the upper and lower yield stress are also linearly dependent of temperature, and again, with a constant yield drop. Such behavior implies that the yield kinetics are governed by only one molecular relaxation process in this range of conditions. This type of kinetics are well described by the Eyring flow theory [10]. This theory describes the jump of segments of macromolecules over a potential barrier, causing plastic flow. Here, the Eyring relation is written in terms of strain rate and temperature:

$$\sigma(\dot{\varepsilon}, T) = \frac{kT}{V^*} \sinh^{-1}\left[\frac{\dot{\varepsilon}}{\dot{\varepsilon}_0} \exp\left(\frac{\Delta U}{RT}\right)\right], \tag{2.1}$$

where V^* is the activation volume which determines the stress dependence, ΔU is the activation energy which determines the temperature dependence, $\dot{\varepsilon}_0$ is a rate constant, R the universal gas constant, k is Boltzmann's constant and T the absolute temperature. The fact that this relation reflects linear behavior, on the one hand as a function of the logarithm of the strain rate, on the other as a function of temperature, becomes clear when realizing that for large x, $\sinh^{-1}(x) \approx \ln(2x)$. For the strain rate dependence, the slope is determined by the activation

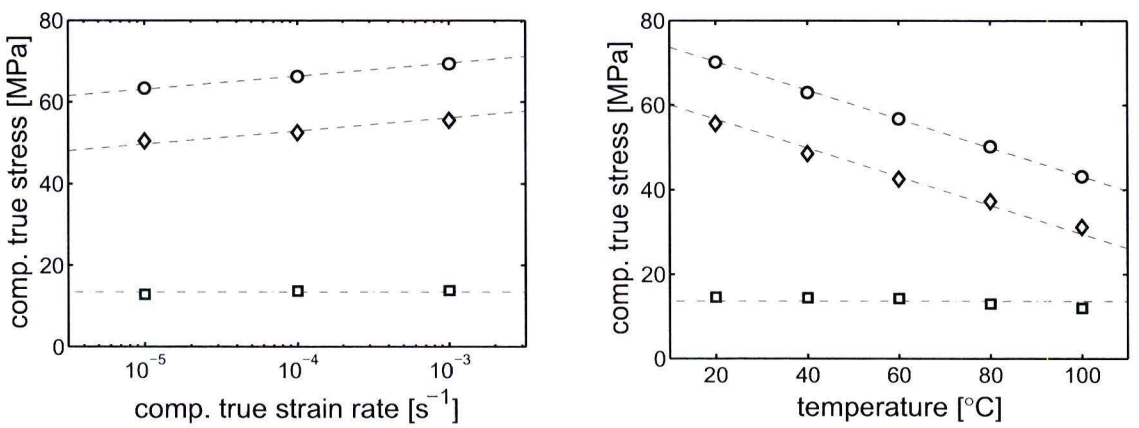

Figure 2.2: Yield stress, lower yield stress, and yield drop for the data from Figure 2.1, as a function of (a) true strain rate and of (b) temperature.

volume V^*, while the activation energy ΔU describes the dependence of temperature. For the dependence of temperature, this distinction is somewhat less clear, as here the slope is determined by both the activation volume, the strain rate, and the rate constant $\dot{\varepsilon}_0$, while the ratio of activation energy and activation volume gives the stress at absolute zero.

Thermorheological complex behavior

It has long been known that for many polymers multiple molecular relaxation mechanisms are actively contributing to the deformation behavior. This is also the case for polycarbonate. At room temperature and moderate strain rates, only one process contributes to the yield kinetics, see Figure 2.2a. This is commonly referred to as the α process, which is associated with the primary glass transition. For high strain rates and/or for temperatures well below room temperature a transition is observed. A second process comes into play, marked by a distinct change in slope, see Figure 2.3, which will be referred to as the β-process. This phenomenon was already reported

by Roetling [22] and Bauwens-Crowet *et al.* [2]. They used the Ree-Eyring modification [21] of Eyring's theory to describe this occurrence of multiple processes, which assumes that at the same average rate, the stresses are additive:

$$\sigma = \sigma_\alpha + \sigma_\beta. \tag{2.2}$$

The expressions for the stress contributions of the α and β processes are similar to that in Equation (2.1), but now with parameters describing the time-temperature behavior of the individual processes:

$$\sigma_x = \frac{kT}{V_x^*} \sinh^{-1}\left[\frac{\dot{\varepsilon}}{\dot{\varepsilon}_{0,x}} \exp\left(\frac{\Delta U_x}{RT}\right)\right] \qquad \text{with} \quad x = \alpha, \beta. \tag{2.3}$$

It is emphasized that the α-process is always present in the deformation kinetics. So depending on the conditions the yield kinetics are either in the α or in the $(\alpha + \beta)$ regime. As an example,

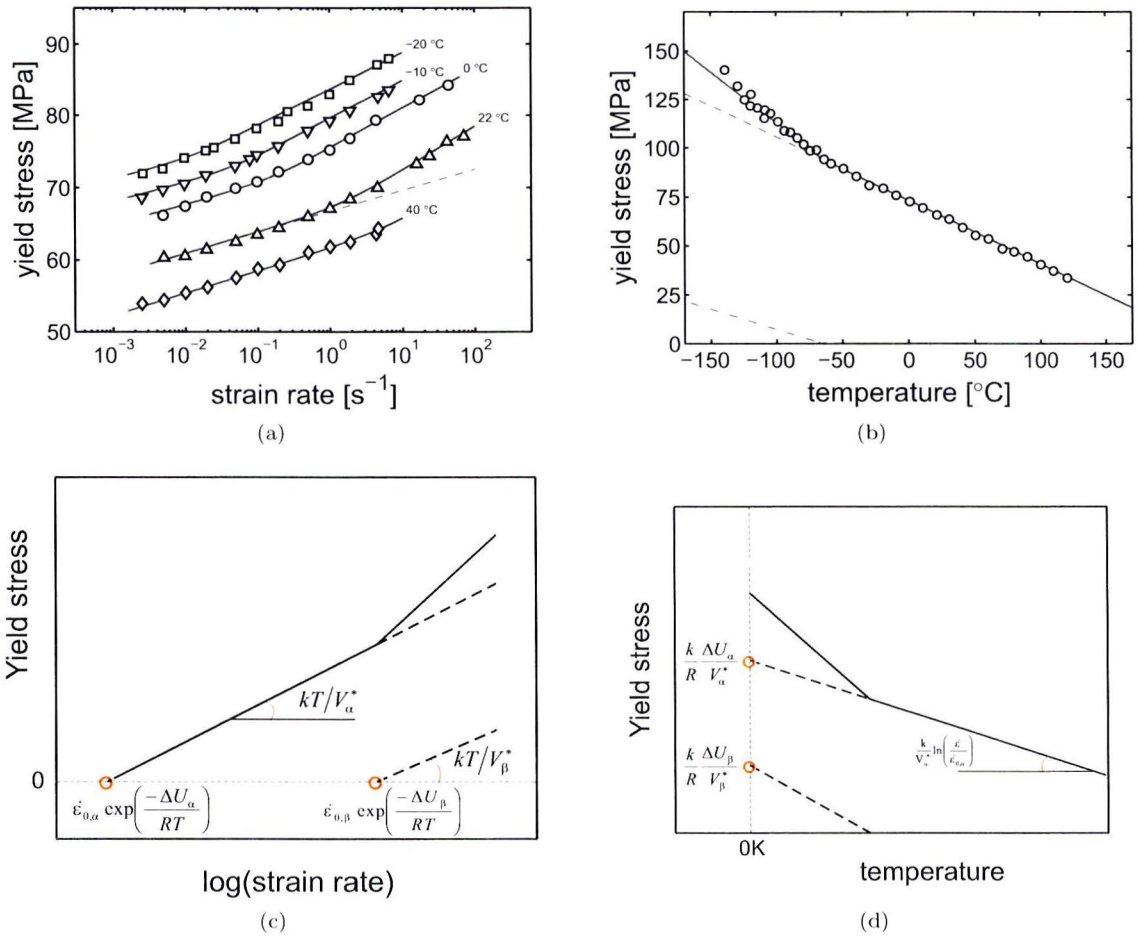

Figure 2.3: Thermorheologically complex behavior of polycarbonate: (a) tensile yield stress as a function of strain rate for various temperatures [17], and (b) tensile yield stress as a function of temperature at $\dot{\varepsilon} = 4.16 \cdot 10^{-3}$ s^{-1} [2]. Symbols represent experimental data and solid lines fits using Equation (2.2) with the parameters from Table 2.1. Dashed lines represent the α-contribution to the total stress. Schematic illustration of the yield stress as a function of (c) strain rate and (d) of temperature, for the Ree-Eyring relation.

Figure 2.3a shows the tensile yield stress of PC as a function of strain rate for a number of different

Table 2.1: Eyring parameters for PC, as used in Figure 2.3.

Figure	x	V_x^* [nm^3]	ΔU_x [kJ/mol·K]	$\dot{\varepsilon}_{0,x}$ [s^{-1}]
2.3a	α	3.21	289.9	$5.76 \cdot 10^{28}$
	β	3.05	64.7	$6.42 \cdot 10^{11}$
2.3b	α	3.21	312	$3.2 \cdot 10^{30}$
	β	3.05	79	$5.8 \cdot 10^{17}$

temperatures, adopted from [17]. At 40°C only one slope is seen over the whole range of strain rates, while at room temperature, with increasing strain rate, a change in slope can be identified. The former is governed by the α-process for the whole experimental range, while the latter shifts from the α to the $(\alpha + \beta)$ regime at $\dot{\varepsilon} \approx 10^0$ s^{-1}. The transition is shifting to lower rates with decreasing temperature. This shift in the transition to lower temperatures can also be visualized by plotting the yield stress as function of temperature, see Figure 2.3b (adopted from Bauwens-Crowet *et al.* [2]), which is actually equivalent to evaluating the data in Figure 2.3a at a constant strain rate. Again, a transition is observed, which suggests that for this particular time scale (i.e. strain rate) the transition occurs at a temperature in the range of -100°C and -50°C. The Eyring parameters used in Equation (2.3) to describe the data in Figure 2.3 are listed in Table 2.1. For Figure 2.3a these where adopted from [17]; for describing the data in Figure 2.3b, the same activation volume was used, while determining the other parameters for best fit results. To clarify the effect of both processes, in Figure 2.3a the fit for room temperature is split up in its α and $(\alpha + \beta)$ contributions. This split is also made in Figure 2.3b, where the dashed line represents the stress contribution from the α-process and the dashed-dotted line that of the β-process. Figures 2.3c and 2.3d give schematic illustrations of the effect of the parameters and variables in the Ree-Eyring relation. Typical expressions for the slopes of the strain rate and temperature dependence, and the asymptotic/theoretical values, are also indicated.

Chapter 3

Phenomenology

In the introduction it was pointed out that the stress response of PC at large strains cannot be properly described by a purely elastic strain hardening contribution; an issue which can be resolved by introducing a deformation dependence in the flow stress. This effect can be quantified by studying the evolution of the deformation kinetics as a function of the (pre)strain. There are basically two ways to do this. The first option is to predeform a sample and subsequently determine its yield kinetics at this level of prestrain. Possible ways to impose this preorientation is by deforming a tensile bar to a specified draw ratio, or cold rolling of sheets to get a specified planar deformation. This method was used by Senden *et al.* [24] on PC tensile bars, that were mechanically rejuvenated so that different levels of prestrain could be homogeneously applied in uniaxial tension. Another option to asses the influence of strain on the deformation kinetics is to take the whole stress-strain response into account. In this method, the rate and temperature dependence is not only evaluated at yield, but its evolution with increasing strain is monitored. Therefore, a distinction is made between between, on the one hand, 'yield kinetics' (i.e. evaluated at yield) and on the other hand deformation kinetics, meaning the exact same kinetics, but now evaluated at an arbitrary level of strain. The method of evaluating the intrinsic behavior itself was previously employed by Wendlandt *et al.* [28], who in this manner investigated the non-linear rate-dependent strain hardening behavior of a number of polymer glasses. However, one disadvantage is that only the large strain regime can be evaluated, because results are otherwise obscured by strain softening.

Despite its disadvantage, in this study the last method will be employed. Main reason for this choice is the availability of the two sets of data depicted in Figure 2.1. Both series of compression testing were done on the same grade of PC with the same history. When comparing these two sets, it is clear that this range of temperatures shows a much wider range of (yield) stresses than the applied range of strain rates, compare Figures 2.1a and 2.1b. Probing deformation kinetics by performing tests at different strain rates has two major limitations. At low strain rates time becomes a limiting factor, as a compression test at 10^{-5} s^{-1} takes about a day to complete. For high strain rates viscous heating of the sample becomes a limiting factor. At higher strains the sample temperature increases, as the amount of heat generated due to energy dissipation during plastic deformation is greater than the amount that is extracted through convection and/or conduction to the environment. This increase in temperature causes the flow stress the decrease, obscuring the results. For these reasons time-temperature superposition is often used: when the experimental time-scale is limited, the characteristic timescale of the relaxation process is shifted by testing at a different temperature. This can also be understood from Equation (2.1), since the strain rate is scaled by the expression $\dot{\varepsilon}_0 \cdot \exp(-\Delta U/RT)$. Here, the activation energy ΔU determines how the characteristic timescale of the relaxation process shifts with temperature. Therefore, the added value of having a data set across a large range of temperatures is evident. Both data sets will be discussed separately in the following paragraphs.

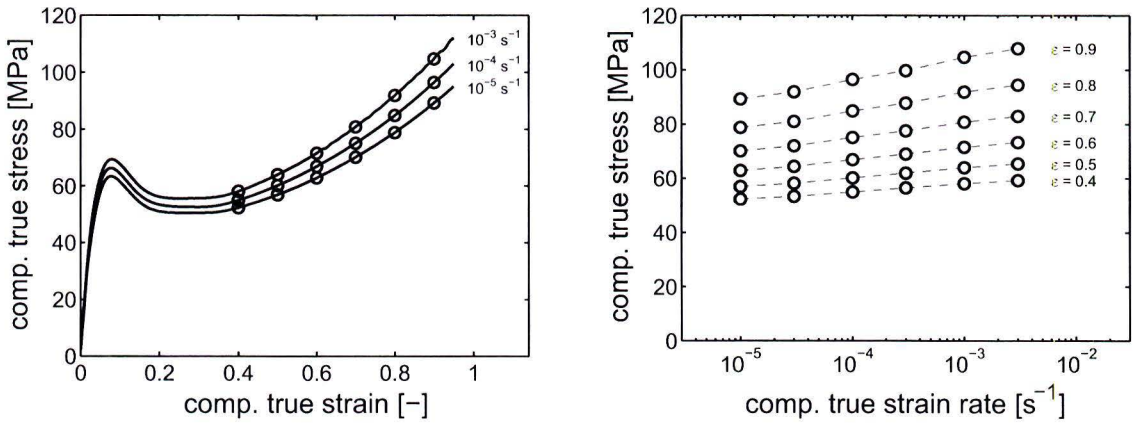

(a) (b)

Figure 3.1: (a) Compression tests on PC at different true strain rates, as depicted in Figure 2.1a. (b) Compressive true stresses at specified strain levels, corresponding with the markers, but now plotted as a function of strain rate. Dashed lines are a guide to the eye.

Strain rate dependent data

In Figure 3.1a the stress-strain response of PC at different strain rates is given. These are actually the same curves as in Figure 2.1a, but now markers are added at evenly spaced intervals for $0.4 \leq \varepsilon \leq 0.9$. In Figure 3.1b,these data points are plotted as a function of the applied strain rate. This clearly gives a similar result as the yield kinetics, compare with Figure 2.2a, as the stress appears to be linearly dependent of the logarithm of strain rate for each level of strain. Furthermore, the slope appears to increase with increasing strain, as suggested by the guides to the eye in Figure 3.1b.

To aid the interpretation of these observations, the Ree-Eyring relation as given in Equation (2.3) will be rewritten in a more convenient form. As for $x \gg 1$, $\sinh^{-1}(x) \approx \ln(2x)$, the Ree-Eyring relation can be rewritten as a linear function of $\ln(\dot{\varepsilon})$:

$$\sigma_x \approx \underbrace{\frac{kT}{V_x^*}}_{\text{(I)}} \ln(\dot{\varepsilon}) - \underbrace{\frac{kT}{V_x^*} \ln\left[\tfrac{1}{2}\dot{\varepsilon}_{0,x} \cdot \exp\left(\frac{-\Delta U_x}{RT}\right)\right]}_{\text{(II)}} \qquad \text{with} \quad x = \alpha, \beta. \tag{3.1}$$

Herein, the part marked (I) represents the slope, and the part marked (II) the constant in the linear relation between stress and logarithm of strain rate; see Figure 2.3c for an illustration of the effect of these parts. Therefore, a strain induced change of slope in the deformation kinetics of a process (at constant temperature) manifests itself as a deformation dependent activation volume $V^*(\varepsilon)$. As it is observed that the slope indeed increases with the strain, this seems to be the case. In fact, Wendlandt *et al.* [28] came to exactly this conclusion. The performance of the Eyring model with a deformation dependent activation volume is visualized in Figure 3.2a, where the experimental data is fitted using a different activation volume for each strain level. Herein, the activation energy of the α-process (Table 2.1,parameters associated with Figure 2.3a) was used, $\dot{\varepsilon}_0$ was fitted on $\varepsilon = 0.4$. Note that in this case a single molecular relaxation mechanism is assumed, which changes with deformation. At the lower strain levels this method obviously works well, but at higher strains the experimental data points are less accurately described. This is caused by the fact that, as the other parameters remain constant, all the lines coincide in a single point at $\sigma = 0$, see Figure 1.1a. Another interpretation of the phenomenon was given by Senden *et al.*, who suggested that, in the case of PC, not the slope of the deformation kinetics itself changes with deformation, but that the observed change in slope is actually caused by a shifting

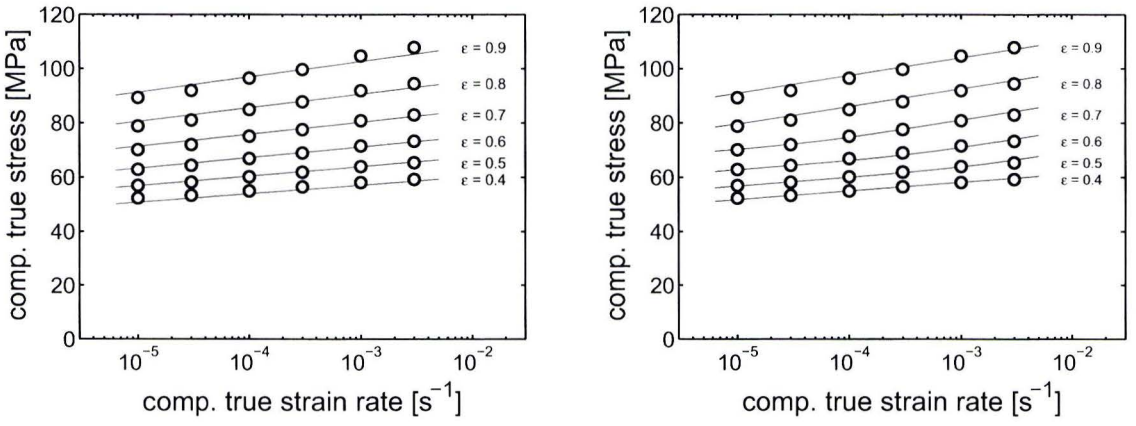

(a) $V^*(\lambda)$ (b) $\dot{\varepsilon}_{0,x}(\lambda)$

Figure 3.2: Compressive true stress at different strain levels as a function of strain rate, see Figure 3.1b. Symbols represent experimental data and solid lines are fits using Equation (3.1) with (a) a deformation dependent activation volume (single process) and (b) deformation dependent rate constants for both the α- and β-process.

of the β-process. This implies that at the least the β rate constant $\dot{\varepsilon}_{0,\beta}$, but in fact also $\dot{\varepsilon}_{0,\alpha}$, are deformation dependent, rather than the activation volume. With deformation, see Figure 1.1b, the moment that the β-process starts playing a role shifts to lower strain rates. This is demonstrated in Figure 3.2b, where Ree-Eyring fits are shown using values of rate constants $\dot{\varepsilon}_{0,\alpha}$ and $\dot{\varepsilon}_{0,\beta}$ that are fitted separately for each strain level. Values for the activation volume and activation energy for both processes were taken from Table 2.1 (parameters associated with Figure 2.3a). At the lower strains, this method also works well, compared to the one previously discussed. At the higher strains (0.7–0.8) it appears to perform somewhat better, but the difference is minimal again at the highest strain depicted. Therefore, as hardly any difference in quality can be distinguished between the predictions from both of these modeling choices, it remains inconclusive which one is correct.

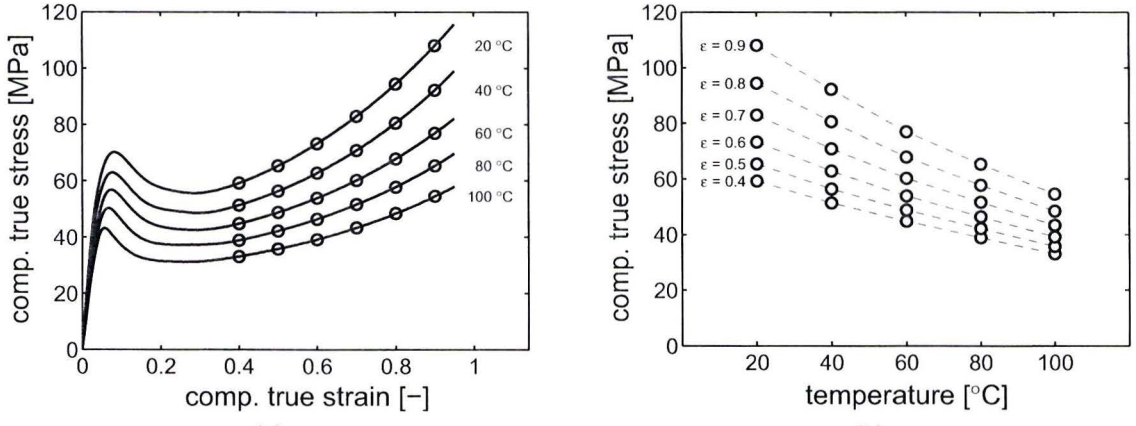

(a) (b)

Figure 3.3: (a) Compression tests on PC at different temperatures, as depicted in Figure 2.1b. (b) Compressive true stresses at specified strain levels, corresponding with the markers, but now plotted as a function of temperature. Dashed lines are a guide to the eye.

Temperature dependent data

With the data at different strain rates alone, see Figure 3.2, it is not possible to identify which modeling choice is correct, as the range of strain rates is insufficient to make the distinction between the kinetics of one process changing with deformation, or the kinetics of two processes shifting with deformation. As mentioned before, compression tests at varying temperatures probe a much wider range of deformation kinetics and provide a lot of additional information on the strain dependence of these kinetics. Therefore, the same procedure as with the compression tests at different strain rates is employed: the compressive stress-strain curves are evaluated at evenly spaced levels of strain, after which these data-points are plotted as a function of temperature, see Figures 3.3a and 3.3b. For the lower strains ($\varepsilon < 0.6$) the stress is linearly dependent of the temperature. At higher strains, however, a transition in the slope can be identified, similar to the behavior found in the yield data of PC by Bauwens-Crowet *et al.*, see Figure 2.3b. This indicates that with deformation, the β-process shifts so that it already starts contributing to the response at higher temperatures. More specifically, it is clear from Figure 3.3b, that the stress response at 20°C starts in the α-regime but gradually shifts to the $(\alpha + \beta)$-regime with increasing strain. As these tests were done at a strain rate of 10^{-3} s^{-1}, this conclusion is also true for the strain rate dependent data: at $\dot{\varepsilon} = 10^{-3}$ s^{-1} it shifts from the α-regime to the $(\alpha + \beta)$-regime with increasing deformation. This means that the activation volumes (i.e. the slopes) are independent of deformation for both processes; the deformation induced changes are caused by a shift of the two processes (i.e. a change in rate constant $\dot{\varepsilon}_{0,x}$), see Figure 3.2b.

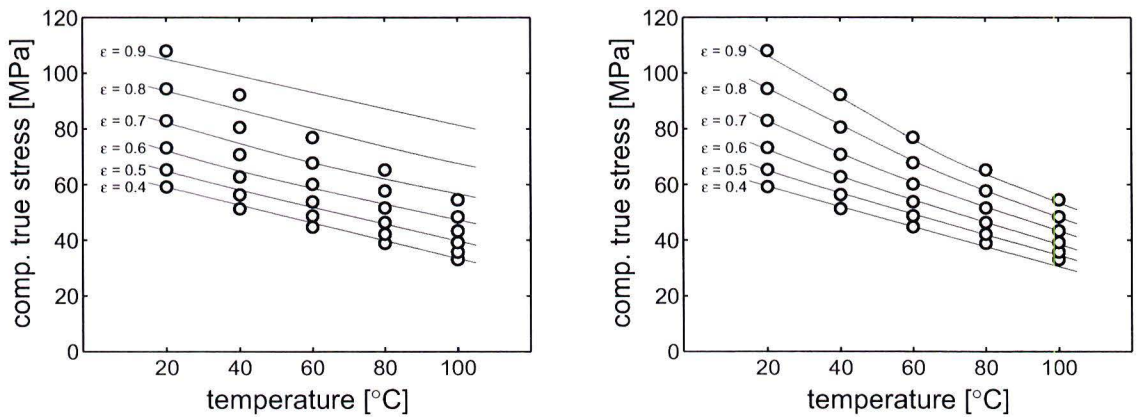

(a) $\dot{\varepsilon}_{0,x}(\lambda)$ (b) $\dot{\varepsilon}_{0,x}(\lambda), \Delta U_x(\lambda)$

Figure 3.4: Compressive true stress at different strain levels as a function of temperature, see Figure 3.3b. Symbols represent experimental data and solid lines are fits using Equation (3.1) with (a) deformation dependent rate constants only and (b) deformation dependent rate constants and activation energies.

Now, the temperature dependent data in Figure 3.3b can also be described using the Ree-Eyring relation. The activation volume and activation energy for both processes are given in Table 2.1 (parameters associated with Figure 2.3a) and the values of $\dot{\varepsilon}_{0,\alpha}$ and $\dot{\varepsilon}_{0,\beta}$ at each strain level are equal to those in the fits of Figure 3.2b. The results are shown in Figure 3.4a. While the data points at 20°C and at the lowest evaluated strain ($\varepsilon = 0.4$) are accurately described,the model does not capture the experimental behavior at all. It even appears that while the data points for each level of strain are converging towards higher temperatures, the predictions are doing the opposite. The reason for this effect is best explained by rewriting the Ree-Eyring relation (Equation (2.3))

again, but now as a linear function of the temperature:

$$\sigma_x \approx \underbrace{\left[\frac{k}{V_x^*}\ln\left(\frac{\dot{\varepsilon}}{\frac{1}{2}\dot{\varepsilon}_{0,x}}\right)\right]}_{\text{(I)}} T + \underbrace{\frac{k}{R}\left[\frac{\Delta U_x}{V_x^*}\right]}_{\text{(II)}} \qquad \text{with} \quad x = \alpha, \beta. \tag{3.2}$$

Herein the part marked (I) represents the slope of the temperature dependence of the stress, which is determined by the strain rate $\dot{\varepsilon}$, the rate constant $\dot{\varepsilon}_{0,x}$ and the activation volume V_x^*. The part marked (II) is the constant offset in the temperature dependence, i.e. the theoretic value of the stress at absolute zero ($T = 0$ K), which is characterized by the ratio of the activation energy and activation volume of the individual processes, see Figure 2.3d. As both of these parameters are considered constants in this case, the predictions all converge to a single stress level towards absolute zero, regardless of the strain level. However, the experimental data suggests that the value of the stress at 0 K increases with deformation, implying that either the activation energy or the activation volume should change with deformation. Because it was previously concluded that the latter does not change with deformation, the conclusion must be drawn that the activation energy is deformation dependent. This means that deformation seems to have a combined time-temperature effect:

$$\dot{\varepsilon}_{0,x}^*(\lambda) = \dot{\varepsilon}_{0,x}(\lambda) \cdot \exp\left(\frac{-\Delta U_x(\lambda)}{RT}\right), \tag{3.3}$$

implying that the fits in Figure 3.2b provide information on $\dot{\varepsilon}_{0,x}^*(\lambda)$, rather than $\dot{\varepsilon}_{0,x}(\lambda)$. The data obtained at varying temperatures shows us how the total effect should be distributed over the rate constant $\dot{\varepsilon}_{0,x}(\lambda)$ and the activation energy $\Delta U_x(\lambda)$. The result is shown in Figure 3.4b, which is clear evidence that, with a deformation dependent rate constant and activation energy, the Ree-Eyring relation describes the experimentally observed influence of deformation on the deformation kinetics across a wide range of temperatures and strain rates.

Chapter 4

Constitutive modeling

It is now established that deformation affects the flow stress, i.e. that strain hardening of glassy polymers is a partly viscous process, and that this can be captured by introducing a deformation dependence in the activation energy and the rate constant. The next step is to integrate these findings in a full, three-dimensional constitutive model that also features an elastic strain hardening contribution, since it was pointed out in the introduction that both contributions are necessary for capturing the strain hardening behavior. Here, the Eindhoven Glassy Polymer (EGP) model is used, as it has proven its capability of describing, but also predicting the mechanical behavior of amorphous polymers [16, 27]. First the basic kinematic relations that are used in the course of this thesis are presented. Then, the multi-process version of the EGP model, as described by Van Breemen [26], are discussed. Finally, the modeling of both the elastic and the viscous contribution to strain hardening are addressed.

4.1 Kinematics

In the EGP model all kinematic representations are based on the concept of a virtual, stress-free intermediate configuration, which implies a multiplicative decomposition of the deformation gradient tensor $\boldsymbol{F}$ into an elastic and a plastic contribution:

$$\boldsymbol{F} = \boldsymbol{F}_e \cdot \boldsymbol{F}_p. \tag{4.1}$$

It is assumed that plastic deformation is incompressible, which implies that the volume change is governed solely by the elastic part of the deformation:

$$J = \det(\boldsymbol{F}) = \det(\boldsymbol{F}_e). \tag{4.2}$$

Non-volumetric deformation is described using the isochoric left Cauchy-Green deformation tensor

$$\tilde{\boldsymbol{B}} = \tilde{\boldsymbol{F}} \cdot \tilde{\boldsymbol{F}}^T, \tag{4.3}$$

where $\tilde{\boldsymbol{F}}$, the isochoric part of the deformation gradient tensor, is defined as $\tilde{\boldsymbol{F}} = J^{-1/3}\boldsymbol{F}$. In an analogous manner the elastic part of the elastic left Cauchy-Green deformation tensor $\tilde{\boldsymbol{B}}_e$ can be calculated. The velocity gradient tensor $\boldsymbol{L}$ can be written as the sum of the symmetric deformation rate tensor $\boldsymbol{D}$ and the skew-symmetric spin tensor $\boldsymbol{\Omega}$. Using the decomposition of $\boldsymbol{F}$ (Equation (4.1)) the velocity gradient tensor $\boldsymbol{L}$ can also be split into an elastic and a plastic velocity gradient tensor.

$$\begin{aligned} \boldsymbol{L} = \dot{\boldsymbol{F}} \cdot \boldsymbol{F}^{-1} &= \dot{\boldsymbol{F}}_e \cdot \boldsymbol{F}_e^{-1} + \boldsymbol{F}_e \cdot \dot{\boldsymbol{F}}_p \cdot \boldsymbol{F}_p^{-1} \cdot \boldsymbol{F}_e^{-1} && (4.4)\\ &= \boldsymbol{L}_e + \boldsymbol{L}_p && (4.5)\\ &= \boldsymbol{D}_e + \boldsymbol{\Omega}_e + \boldsymbol{D}_p + \boldsymbol{\Omega}_p. && (4.6) \end{aligned}$$

A last issue that need to be resolved is that the decomposition of Equation (4.1) is not unique, as it remains undetermined how the total amount of rotation is split in an elastic and a plastic part. It was shown by Boyce *et al.* [5] that this could be solved by taking the plastic spin tensor equal to the null tensor ($\boldsymbol{\Omega}_p = \mathbf{0}$), which implies that the plastic velocity gradient tensor equals the plastic deformation rate tensor: $\boldsymbol{L}_p = \boldsymbol{D}_p$.

4.2 Stress calculation

In the EGP model, the total stress is split into the driving (or flow) stress $\boldsymbol{\sigma}_s$ and the hardening stress $\boldsymbol{\sigma}_r$. The first is attributed to intermolecular interactions that determine the viscoelastic properties at small deformations, and plastic flow; the latter can be interpreted as a rubber elastic contribution of the entanglement network. Here, the multi-process representation of the

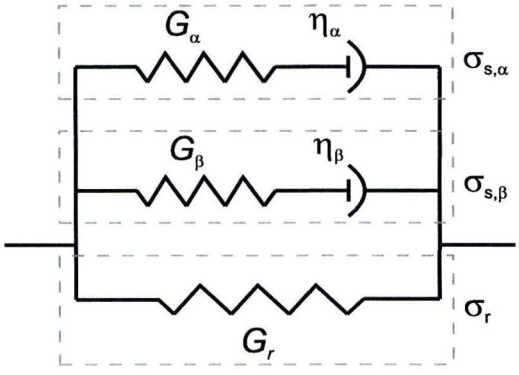

Figure 4.1: Mechanical analogue (1-D) of the multi-process EGP model.

EGP model is discussed, its mechanical analogue depicted in Figure 4.1, as the model material (PC) shows a secondary relaxation mechanism. This implies that the driving stress contains a contribution from the α- and the β-process:

$$\boldsymbol{\sigma} = \underbrace{\boldsymbol{\sigma}^d_{s,\alpha} + \boldsymbol{\sigma}^d_{s,\beta}}_{\boldsymbol{\sigma}_s} + \boldsymbol{\sigma}^h + \boldsymbol{\sigma}^d_r. \tag{4.7}$$

The elastic contribution from the entangled network is modeled with a neo-Hookean relation:

$$\boldsymbol{\sigma}^d_r = G_r \tilde{\boldsymbol{B}}^d, \tag{4.8}$$

governed by the strain hardening modulus G_r. Due to the fact that plastic deformations are assumed to be incompressible, it is assumed that the hydrostatic part of the driving stress depends on the total volume change:

$$\boldsymbol{\sigma}^h_s = \kappa(J-1)\boldsymbol{I}, \tag{4.9}$$

which implies a single bulk modulus κ. The deviatoric part of the driving stress for each process is defined as:

$$\boldsymbol{\sigma}^d_{s,x} = G_x \tilde{\boldsymbol{B}}^d_{e,x} \qquad \text{with} \quad x = \alpha, \beta, \tag{4.10}$$

where G_x denotes the shear modulus and $\tilde{\boldsymbol{B}}^d_{e,x}$ the deviatoric part of the isochoric elastic left Cauchy-Green strain tensor. For each process, the deviatoric driving stress is coupled to the

plastic deformation rate through a non-Newtonian flow rule:

$$\boldsymbol{D}_{p,x} = \frac{\boldsymbol{\sigma}^d_{s,x}}{2\eta_x(T, \bar{\tau}_x, p, S_x)} \qquad \text{with} \quad x = \alpha, \beta. \tag{4.11}$$

As indicated in Equation (4.11), the viscosity of each relaxation process depends on its equivalent stress $\bar{\tau}_x$, pressure p, temperature T, and the thermomechanical state of the material S_x, which includes the effect of intrinsic strain softening.

$$\eta_x = \eta_{0,x} \underbrace{\exp\left(\frac{\Delta U_x}{RT}\right)}_{\text{(I)}} \underbrace{\frac{\bar{\tau}_x/\tau_{0,x}}{\sinh(\bar{\tau}_x/\tau_{0,x})}}_{\text{(II)}} \underbrace{\exp\left(\frac{\mu_x p}{\tau_{0,x}}\right)}_{\text{(III)}} \underbrace{\exp\left(S_x(\bar{\gamma}_p)\right)}_{\text{(IV)}} \tag{4.12}$$

The temperature dependence (part I) is governed by the activation energy ΔU_x; part II represents the stress dependence with characteristic stress $\tau_{0,x}$; the pressure dependence part III is governed by the parameter μ_x; in part IV the state parameter S_x is a function of the equivalent plastic strain $\bar{\gamma}_p$. Part I and II are based on Eyring's flow relation (compare with Equation (2.3)), part III and IV result from an extension of the model by Govaert *et al.* [13]. The initial viscosity is denoted by $\eta_{0,x}$. The characteristic stress $\tau_{0,x}$, pressure p_x, and equivalent stress $\bar{\tau}_x$ are defined as:

$$\tau_{0,x} = \frac{kT}{V^*_x}, \tag{4.13}$$

$$\bar{\tau}_x = \sqrt{\tfrac{1}{2}\boldsymbol{\sigma}^d_{s,x} : \boldsymbol{\sigma}^d_{s,x}}, \tag{4.14}$$

$$p = -\tfrac{1}{3}\mathrm{tr}(\boldsymbol{\sigma}), \tag{4.15}$$

where the activation volume V^*_x governs the temperature dependence of the characteristic stress. It is stressed that this is not the same activation volume as the one presented in the Eyring model. The reason for this confusion is that the characteristic stress in the Eyring relation (defined as kT/V^* in Equation (2.3)) is a uniaxial stress measure, whereas the characteristic in the EGP model (τ_0 as defined in Equation (4.13)) is a pressure modified, shear-equivalent stress measure.

As mentioned before, the state parameter S_x only depends on the equivalent plastic strain, and its evolution is described as follows:

$$S_x = S_{0,x}\left[\frac{1 + (r_{0,x} \cdot \exp(\bar{\gamma}_{p,\alpha}))^{r_{1,x}}}{1 + r_{0,x}^{r_{1,x}}},\right]^{\frac{r_{2,x}-1}{r_{1,x}}} \tag{4.16}$$

where the parameters $r_{x,i}$ $(i = 0, 1, 2)$ govern the kinetics of intrinsic strain softening, which can be different for each process involved. The initial (thermodynamic) state is defined by $S_{0,x}$ and depends on the thermo-mechanical history. As can be seen in Equation (4.12), the state parameter is given as a function of the equivalent plastic strain, which is assumed to be coupled to the process with the highest initial viscosity, in this case the α process. The evolution of the equivalent plastic strain is defined as follows:

$$\dot{\bar{\gamma}}_p = \sqrt{2\boldsymbol{D}_{p,\alpha} : \boldsymbol{D}_{p,\alpha}}. \tag{4.17}$$

Up to now, a single relaxation mechanism (single-mode) for each process is assumed. However, for PC both the pre-yield behavior and the transition at yield from elastic to (visco)plastic behavior is described poorly with such a single mode implementation. Therefore, the model can be extended to account for multiple relaxation times (multi-process). This extension is straightforward, see Van Breemen *et al.* [27]; similar to the multi-process approach (Figure 4.1), the deviatoric part

of the driving stress of each process is modeled as a set of parallel Maxwell elements. The multi-mode approach should, however, not be confused with the concept of multiple processes, as for the former the relaxation kinetics are the same for all modes, whereas for the latter, these kinetics are essentially different for each process.

4.3 Strain hardening: elastic contribution

It is clear that the large-strain response of glassy polymers is governed by an interplay between elastic and viscous strain hardening. Before introducing a viscous contribution to strain hardening in the EGP model, a closer look is taken at the elastic contribution. As mentioned before this elastic part is modeled with a neo-Hookean relation, see Equation (4.8), which in the case of uniaxial loading is represented by a linear relation between stress and $|\lambda^2 - \lambda^{-1}|$, where λ denotes the draw ratio. In Figure 4.2, the stress response of a mechanically preconditioned tensile bar of

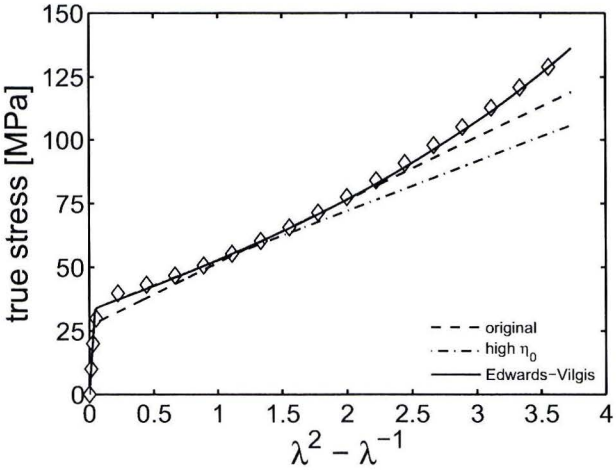

Figure 4.2: Comparison of neo-Hookean and Edwards-Vilgis model for strain hardening in the EGP framework. Symbols represent experimental results in tensile from a mechanically preconditioned sample of PC, data taken from [24]. Predictions using the neo-Hookean model with low initial viscosity (dashed line) and high initial viscosity (dashed-dotted line), parameters taken from [16]. Solid line is prediction using Edwards-Vilgis theory for strain hardening. In all predictions total rejuvenated state is assumed ($S_0 = 0$).

PC is depicted [24]. This preconditioning consists of a large strain torsion of the axisymmetric tensile bar, after which it is twisted back to its original position. The reason for this treatment is to eliminate strain softening, ensuring homogeneous deformation of the sample in a tensile test. In modeling terms, this can be regarded as a removal of the initial age S_0 of the sample, see Equation (4.16), bringing it to a rejuvenated state ($S_0 = 0$). Indeed, when plotting the mechanical response as a function of $(\lambda^2 - \lambda^{-1})$, see Figure 4.2, strain softening seems to be eliminated by the preconditioning.

In the same figure the dashed line represents a simulation of the experiment with the EGP model, using parameters representative for PC, as determined by Klompen *et al.* [16]. These include a strain hardening modulus of $G_r = 26$ MPa, equal to the one determined by Tervoort and Govaert [25]. It is clear that the neo-Hookean model is not capable of describing the whole range of the stress-strain response. The deviation at yield was actually attributed to incomplete rejuvenation of the sample ($S_0 \neq 0$). The origin of this 'residual age' is the fact that predeformation is not homogeneously distributed as the central fiber of the sample does not deform at all. Recent simulation results [23], however, show that this effect of the incompletely rejuvenated core on the total

mechanical response is minimal, implying that the experimentally observed response as shown in Figure 4.2 truly reflects the rejuvenated response of the material. Therefore, it is suggested that a higher initial viscosity should be used to describe the stress at yield more accurately. This is shown in Figure 4.2 by the dash-dotted line, where $G_r = 20.5$ MPa was used to capture the stress response at large strains. Indeed the yield stress is captured more closely now, but it introduces a new problem as well, since it performs even worse than the previous prediction at high strains.

To resolve these problems, the use of another hyperelastic model is proposed: the cross-link slip-link model of Edwards and Vilgis [7], which is also used to describe elastic strain hardening in the Oxford Glass-Rubber (OGR) model [6]. Edwards-Vilgis' theory of rubber elasticity is, in its original form, based on two categories of interaction between molecules: slip-links (entanglements) and cross-links. In the case of glassy polymers the last contribution is omitted, because no cross-links are present. This leads to the following expression for the conformational free energy [19]:

$$W = \tfrac{1}{2} N_s kT \left[\frac{(1+\eta_*)(1-\alpha_*^2)}{1-\alpha_*^2 \sum_{i=1}^{3} \tilde{\lambda}_i^2} \sum_{i=1}^{3} \frac{\tilde{\lambda}_i^2}{1+\eta_* \tilde{\lambda}_i^2} + \sum_{i=1}^{3} \ln(1+\eta_* \tilde{\lambda}_i^2) + \ln\left(1-\alpha_*^2 \sum_{i=1}^{3} \tilde{\lambda}_i^2\right) \right], \quad (4.18)$$

where N_s represents the number density of slip-links, α_* and η_* represent the degree of inextensibility of the chains and the freedom of movement of the slip-links, respectively, and k is Boltzmann's constant. The free energy is written in terms of the principal stretch ratios $\tilde{\lambda}_i$ $(i = 1, 2, 3)$, which are the eigenvalues of the isochoric left stretch tensor $\tilde{\boldsymbol{V}}$, as it is defined by the left polar decomposition of the deformation gradient tensor: $\tilde{\boldsymbol{F}} = \tilde{\boldsymbol{V}} \cdot \boldsymbol{R}$. As shown in Appendix C, equation (4.18) can also be written in tensor notation, as a function of $\tilde{\boldsymbol{B}}$:

$$W = \tfrac{1}{2} G_r \left[\frac{(1+\eta_*)(1-\alpha_*^2)}{1-\alpha_*^2 \mathrm{tr}(\tilde{\boldsymbol{B}})} \mathrm{tr}\left(\tilde{\boldsymbol{B}} \cdot (\boldsymbol{I} + \eta_* \tilde{\boldsymbol{B}})^{-1}\right) + \mathrm{tr}\left(\ln(\boldsymbol{I} + \eta_* \tilde{\boldsymbol{B}})\right) + \ln\left(1-\alpha_*^2 \mathrm{tr}(\tilde{\boldsymbol{B}})\right) \right], \quad (4.19)$$

which is more convenient as it eliminates the necessity of calculating the eigenvalues and eigenvectors of this tensor. Note that the term $N_s kT$ is replaced with a constant strain hardening modulus G_r, as this elastic strain hardening contribution is assumed to be independent of temperature. This assumption is consistent with the original EGP model, where the entropic nature of the neo-Hookean relation was also ignored, see Equation (4.8). The Cauchy stress response of the Edwards-Vilgis model can be derived from hyperelasticity theory:

$$\boldsymbol{\sigma} = \frac{2}{J} \boldsymbol{F} \cdot \frac{\partial W}{\partial \boldsymbol{C}} \cdot \boldsymbol{F}^T. \quad (4.20)$$

For the exact derivation of the stress from the free energy function the reader is referred to Appendix C. Finally, it is noteworthy that for the special case of $\alpha_* = \eta_* = 0$, the response this model coincides with a neo-Hookean response.

Table 4.1: Edwards-Vilgis parameters used in Figure 4.2

G_r [MPa]	α_* [-]	η_* [-]
14.6	0.255	0

In Figure 4.2, the solid line depicts the response of the EGP model, using the theory of Edwards-Vilgis to describe the elastic strain hardening behavior. The Edwards-Vilgis parameters are listed in Table 4.1. As discussed in the Introduction, the entanglement network remains intact for glassy polymers that are plastically deformed below the glass transition temperature T_g, implying that there is no freedom of movement of the slip-links: $\eta_* = 0$. Now only the α_*-parameter determines how the response of the model deviates from neo-Hookean behavior, this being a more pronounced upswing in stress that ultimately leads to infinite stress, i.e. finite extensibility. It

is clear from Figure 4.2 that this model is excellently capable of describing the experimentally observed behavior, both at large strains and around yield. As the neo-Hookean model fails at describing these simultaneously, this is a significant improvement.

4.4 Strain hardening: viscous contribution

In Chapter 3 it was established that (at least) part of the strain hardening effect originates from a deformation dependence the flow stress. Therefore, an extension of the EGP model is required in the form of a deformation dependence in the viscosity. Because deformation in the EGP model is expressed in terms of the isochoric left Cauchy-Green deformation tensor $\tilde{\boldsymbol{B}}$, it seems the obvious choice for modeling this deformation dependence. Of course, a scaled invariant function $f(\tilde{\boldsymbol{B}})$ should be used, as the viscosity is a scalar property. This results in the following flow rule:

$$\boldsymbol{D}_{p,x} = \frac{\boldsymbol{\sigma}^d_{s,x}}{2\eta_x(T, \bar{\tau}_x, p, S_x, f(\tilde{\boldsymbol{B}}))}, \tag{4.21}$$

where the viscosity is extended with this deformation dependence, compared to Equation (4.11). Before actually characterizing this deformation dependence in the viscosity, it is first established what form the invariant function $f(\tilde{\boldsymbol{B}})$ should have. Therefore, viscosity, see Equation (4.12), is expressed in a more simplified form:

$$\eta = \frac{\eta_0^*}{\tau_0} \frac{\bar{\tau}}{\sinh(\bar{\tau}/\tau_0)}, \tag{4.22}$$

where η_0^* contains the temperature, pressure, and state dependent contributions to the viscosity:

$$\eta_0^* = \eta_0 \exp\left[\frac{\Delta U}{RT} + \frac{\mu p}{\tau_0} + S(\bar{\gamma}_p)\right]. \tag{4.23}$$

When introducing a deformation dependence in the viscosity, basically two options are at hand: it can be introduced in the prefactor of Equation (4.22), or in the argument of the hyperbolic sine. In both cases, however, it is merely a scaling of the equivalent stress $\bar{\tau}$. As concluded in the previous section, strain hardening can be accurately described with an Edwards-Vilgis relation. Nevertheless, for reasons of simplicity the neo-Hookean model, see Equation (4.8), will be used as a starting point here. This choice is motivated by the fact that in the limit of $\alpha_* = \eta_* = 0$, the repsonse of the Edwards-Vilgis model equals that of the neo-Hookean model.

Now, by substituting the (deviatoric) neo-Hookean stress in the definition for the equivalent stress (Equation (4.14)), a deformation dependence of the equivalent stress can be deduced that exhibits neo-Hookean type behavior:

$$\bar{\tau} = \sqrt{\tfrac{1}{2}\boldsymbol{\sigma}^d : \boldsymbol{\sigma}^d} \qquad \boldsymbol{\sigma}^d = G_r \tilde{\boldsymbol{B}}^d \tag{4.24}$$

$$\begin{aligned} \bar{\tau} &= G_r \sqrt{\tfrac{1}{2}\tilde{\boldsymbol{B}}^d : \tilde{\boldsymbol{B}}^d} \\ &= G_r f(\tilde{\boldsymbol{B}}). \end{aligned} \tag{4.25}$$

After rearrangement, this results in the following expression:

$$f(\tilde{\boldsymbol{B}}) = \sqrt{\tfrac{1}{3} I_{\tilde{\boldsymbol{B}}}^2 - II_{\tilde{\boldsymbol{B}}}}. \tag{4.26}$$

Since the viscosity is characterized by scaling of the equivalent stress, and this equivalent stress in turn is proportional to $f(\tilde{\boldsymbol{B}})$, the same proportionality exists between this function and the viscosity. In Chapter 3 it was concluded that both the rate constant and the activation volume change with deformation. A deformation-induced change in the rate constant is equivalent to

a change in initial viscosity, since $\eta_0 = \tau_0/\dot{\gamma}_0$, where τ_0 is deformation independent and $\dot{\gamma}_0$ is the shear equivalent of the rate constant $\dot{\varepsilon}_0$. This leads to the conclusion that the deformation dependence manifests itself in the prefactor of Equation (4.22), or more specifically:

$$\eta_0 \propto f(\tilde{\boldsymbol{B}}) \quad \text{and} \quad \exp(\Delta U) \propto f(\tilde{\boldsymbol{B}}). \tag{4.27}$$

It is of course possible to do the same procedure with the Edwards-Vilgis theory, but this would needlessly complicate both the model equations and the characterization of the moel with experimental data. This quantitative characterization and its application in the EGP model is the subject of the next chapter.

Chapter 5

Simulation results

In the previous chapter the general framework of the EGP model and the modeling of strain hardening as a combination of an elastic and a viscous contribution were discussed. Here, these findings are further investigated via numerical simulations. First, the elastic and viscous contributions to strain hardening are characterized. After that, the performance of the model is assessed by comparing numerical simulations with experimental data.

5.1 Model characterization

Ratio of strain hardening contributions

The first step is to determine what part of the total strain hardening originates from the elastic contribution. An answer to this question was presented by Senden *et al.* [Senden2010], who investigated the relation between the Bauschinger effect in oriented polymers and strain hardening. Their leading observation is reproduced in Figure 5.1, where the mechanical response of

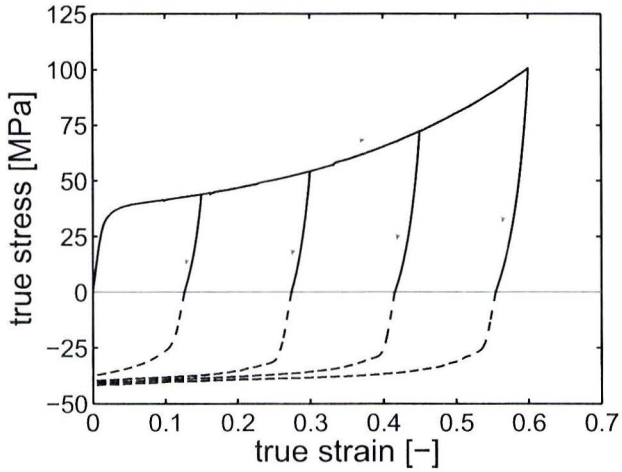

Figure 5.1: An impression of the mechanical response of PC in cyclic, i.e. tension up to a certain strain and then compression back to its original length, uniaxial deformation. Data taken from [24].

mechanically preconditioned samples of PC is depicted. As previously discussed in Section 4.3, the main reason for applying this preconditioning is to ensure homogeneous deformation in tension. First, the specimen was loaded in tension with a constant true strain rate up to a predefined true strain level, after which the load was removed. This was done for several different strain levels.

Next, cylindrical specimens were machined from these preoriented tensile bars to perform uniaxial compression tests at the same absolute true strain rate. The results were combined with those of the tensile tests to give an impression of the actual behavior of PC when subjected to a cyclic loading path. This is illustrated in Figure 5.1, where the solid lines represent the tensile stage and the dashed lines the compression tests. It is clear that, especially at high preorientation, a strong Bauschinger effect occurs: at a prestrain of 0.6 the momentary yield stress in tension is approximately 100 MPa, whereas the corresponding yield stress in compression is only -25 MPa. After yield, the compressive stress response remains nearly constant at approximately 40 MPa, a value that is similar to the initial yield stress in tension.

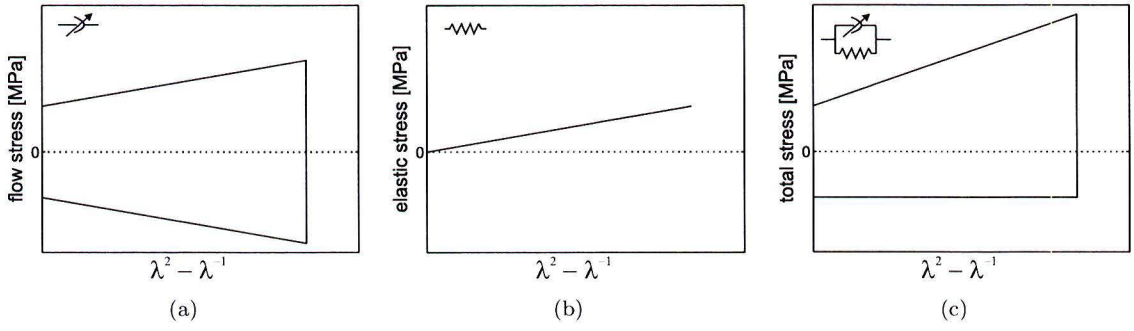

Figure 5.2: Schematic representation of the stress contributions during a tension/compression cycle: (a) deformation dependent viscous contribution, (b) elastic contribution to strain hardening, and (c) the total stress. Stress are as a function of $\lambda^2 - \lambda^{-1}$, implying neo-Hookean stress response.

Senden *et al.* investigated the implications of modeling strain hardening as a partly elastic, partly viscous process with a simple *gedankenexperiment*. The concept is based on a simplified model, focussing only on the post-yield response, as schematically illustrated in Figure 5.2. Due to the introduction of viscous strain hardening, the viscous contribution to the stress, see Figure 5.2a, continues to increase with deformation after yield. When the deformation direction is reversed, the compressive yield stress is of equal magnitude, but opposite in sign compared to the level of stress just before load reversal; its magnitude decreases with further deformation. The elastic component, see Figure 5.2b, naturally follows the same curve during tensile loading as during compressive loading. Finally, in Figure 5.2c the total stress response is depicted, being the sum of the two contributions. In the tensile stage of the loading path, these two contributions together determine the total stress increase after yield. After reversal of the loading direction, however, only the flow stress changes sign. In the case of an equal distribution of elastic and viscous strain hardening, the two strain hardening contributions cancel each other out, resulting in a constant stress level for the remainder of the compression stage in the cycle. This is exactly the type of behavior that is observed in experiments (Figure 5.1), indicating that the elastic and viscous strain hardening should indeed be of equal magnitude.

Quantifying the viscous strain hardening contribution

Quantifying the viscous contribution to strain hardening boils down to a characterization of the deformation dependence of the flow stress. As it is now known what portion of the strain hardening effect originates from the elastic contribution, this part can be subtracted from the experimental data, isolating the flow stress. This is actually the same procedure as performed in Chapter 3, but now on the flow stress only, instead of the total stress. Assuming incompressibility, and the same pressure dependence for both processes, the 1-D stress response of the EGP model can be derived, see Appendix B.

$$\sigma = \sigma_{flow} + \sigma_{elast.}, \tag{5.1}$$

$$\sigma_{flow} = \frac{-3}{\sqrt{3}-\mu} \sum_{x=\alpha,\beta} \frac{kT}{V_x^*} \ln\left[2\sqrt{3}\dot{\varepsilon}\frac{V_x^*}{kT}\eta_{0,x}\exp\left(\frac{\Delta U_x}{RT}\right)\right] \qquad \text{with} \quad x=\alpha,\beta, \tag{5.2}$$

$$\sigma_{elast.} = \frac{\sqrt{3}}{\sqrt{3}-\mu} G_r \cdot h(\lambda, \alpha_*). \tag{5.3}$$

Herein, the function $h(\alpha_*, \lambda)$ signifies the 1-D strain dependence of the Edwards-Vilgis model (Equation (B.4)), where in the absence of mobility in the slip-links, the parameter η_* is omitted. Using Equation (5.3), the elastic strain hardening contribution can be subtracted from the total stress-strain response of a compression test. This procedure is done for the experimental data

Table 5.1: Edwards-Vilgis parameters.

G_r [MPa]	α_* [-]	η_* [-]
7.0	0.25	0

depicted in the Figures 3.1 and 3.3, using parameters from Table 5.1. The parameters given here do not constitute an exact 50% elastic strain hardening contribution, compared to those given in Table 4.1, for reasons that become clear later on. The results from these elastic strain hardening corrections are shown in Figure 5.3. Note that for each level of strain a fixed amount of stress is subtracted.

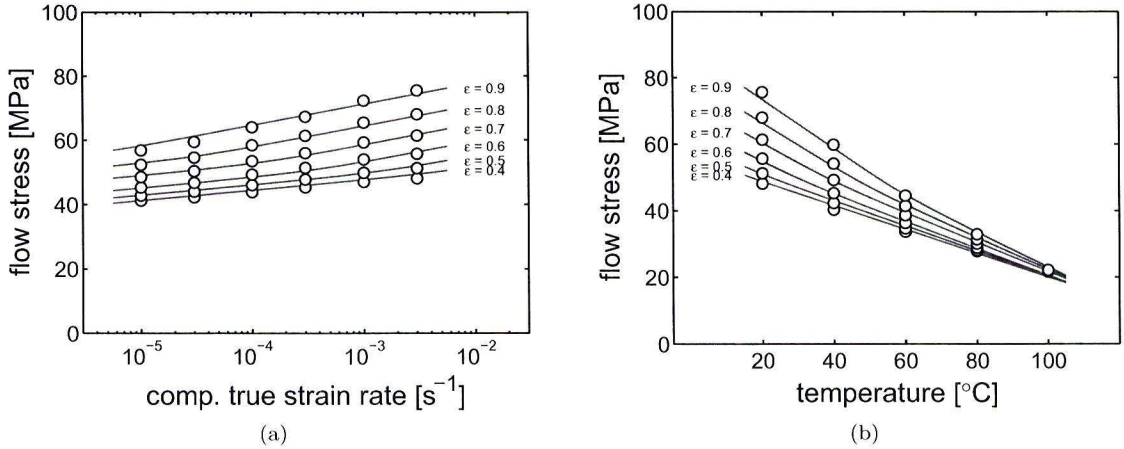

Figure 5.3: Compressive flow stress at different strain levels, stresses are corrected for elastic contribution in strain hardening (symbols), as a function of (a) compressive true strain rate and (b) temperature. Solid lines are fits using Equation (5.2), fit parameters are listed in Table 5.2.

For the tests at varying strain rates, see Figure 5.3a, the overall picture is similar to that in Figure 3.1b, although the stresses have decreased in such a way that the lines corresponding to different levels of strain are closer to one another. The changes look more striking for the tests at different temperatures (Figure 5.3b), as the data suggests that at a temperature of 100°C the viscous contribution to the strain hardening is negligible, compare with Figure 3.3b. Next, the evolution of the initial viscosity $\eta_{0,x}$ and that of the activation energy ΔU_x can be determined, using Equation (5.2). The combined effect of these parameters is expressed by:

$$\eta_{0,x}^*(\lambda, T) = \eta_{0,x}(\lambda)\exp\left(\frac{\Delta U_x(\lambda)}{RT}\right). \tag{5.4}$$

From Figure 5.3a values of $\eta^*_{0,x}$ at each strain level can be deduced, as this data is obtained at constant temperature. Subsequently, the data obtained at varying temperatures, see Figure 5.3b, provide how the deformation dependence of $\eta^*_{0,x}$ is distributed over the two parameters $\eta_{0,x}$ and ΔU_x. In Table 5.2 the parameters are listed which were used during this procedure. The

Table 5.2: Parameters describing flow stress in Figure 5.3.

V^*_α [nm^3]	V^*_β [nm^3]	$\mu_{\alpha,\beta}$ [-]	$\eta_{0,x}$ [MPa·s]	ΔU_x [kJ/mol·K]
5.32	5.06	0.08	Figure 5.4a	Figure 5.4b

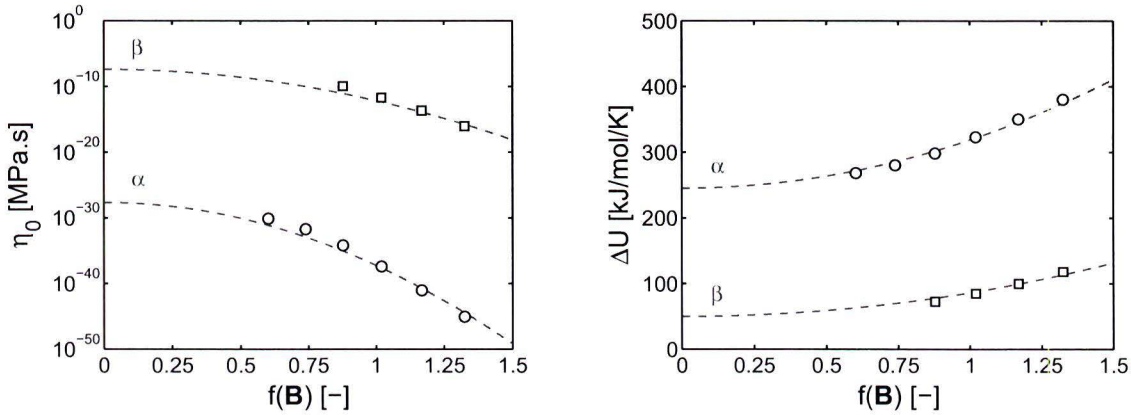

Figure 5.4: Evolution in the deformation dependence of (a) the initial viscosity $\eta_{0,x}$ and (b) the activation energy ΔU_x, both for the α-process ($\circ$) and β-process ($\square$), as a function of viscous hardening function $f(\boldsymbol{B})$. Dashed lines are fits using Equations (5.5) and (5.6).

resulting values of the initial viscosity as well as the activation energy are shown in Figure 5.4, for both the α- and the β-process. For the latter, only large strain levels could be evaluated, since the contribution of the β-process could not be clearly recognized at smaller strains. Values are plotted as a function of $f(\boldsymbol{B})$, which was derived in the previous chapter as the characteristic strain function for the viscous strain hardening contribution. Note that in Figure 5.4a the initial viscosity actually decreases with deformation, whereas the total viscosity increases. This is due to the increasing activation energy, which contributes exponentially to the viscosity, see Equation (5.4). To a good approximation, the values of initial viscosity and activation energy are described with a quadratic function $f^2(\boldsymbol{B})$:

$$\eta_{0,x}(f(\boldsymbol{B})) = \eta_{0,x} \cdot \exp\left(C_{1,x} f^2(\boldsymbol{B})\right), \tag{5.5}$$

$$\Delta U_x(f(\boldsymbol{B})) = \Delta U_{x,0} + C_{2,x} f^2(\boldsymbol{B}). \tag{5.6}$$

Herein, $C_{1,x}$ is introduced, controlling the evolution of the initial viscosity, and $C_{2,x}$, which governs the evolution of the activation energy as a function of strain. The parameters that result from fitting the data in Figure 5.4 using Equations (5.5) and (5.6) are listed in Table 5.3. The values of the initial activation energies found here are somewhat smaller compared to the ones determined using yield data (Table 2.1). This might be caused by the function that was used to fit the evolution of $\Delta_{U,x}$ (Equation (5.6)). It remains difficult to determine the exact cause as the observations are obscured by strain softening around yield.

Table 5.3: Fit parameters from Equations (5.5) and (5.6)

x	$\eta_{0,x}$ [MPa·s]	$C_{1,x}$ [-]	$\Delta U_{x,0}$ [kJ/mol·K]	$C_{2,x}$ [kJ/mol·K]
α	$2.1 \cdot 10^{-28}$	-22.0	245	73.7
β	$4.0 \cdot 10^{-8}$	-11.0	50	36.3

5.2 Simulation results

With the characterization of the deformation induced evolution for both the initial viscosity and the activation energy, all ingredients are available to test the performance of the proposed modifications of the EGP model. For this purpose, numerical simulations are performed using the finite element package MSC.Marc; the user subroutine HYPELA2 is used to implement the constitutive model. Uniaxial testing is simulated using a single linear quadrilateral axisymmetric element. Here, the α-process is modeled with multiple relaxation times (Section 4.2) as described by Van Breemen *et al.* [27]; the β-process is described by a single-mode.

Most parameters for PC, including the relaxation spectrum for the α-process, are adopted from Van Breemen *et al.* [27], with the exception of those originating from this work. The initial viscosities in the relaxation spectrum $\eta^*_{0,x}(T)$ had to be converted to the temperature independent one ($\eta_{0,x} = \eta^*_{0,x}(T) \cdot \exp(-\Delta U_0/RT)$), as these were originally determined for a single temperature. Furthermore, the spectrum is adopted to account for the larger (total) initial viscosity needed due to the switch to the elastic strain hardening from Edwards-Vilgis' theory, see Section 4.3. Input parameters, including the adapted relaxation spectrum for the α-process, are listed in Appendix A. Note that only a single mode is used for the β-process.

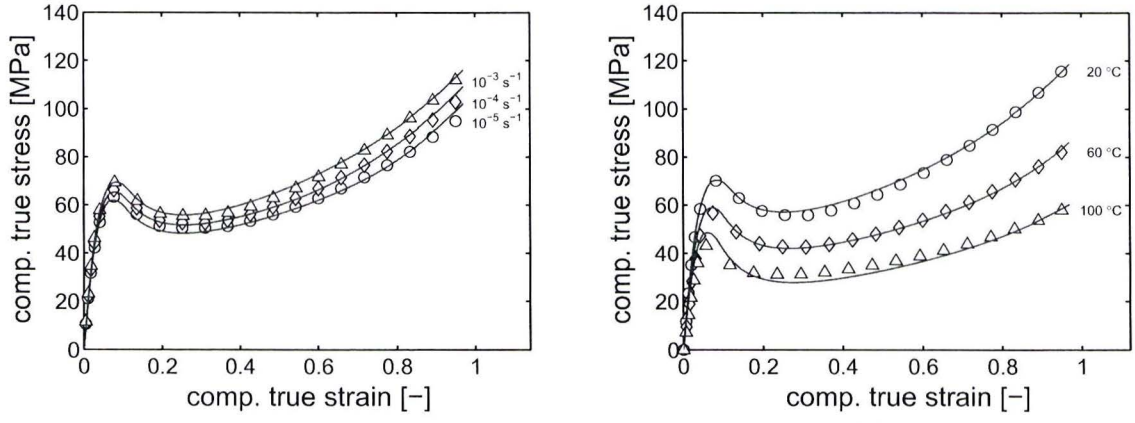

(a) (b)

Figure 5.5: Compression testing of PC. Symbols represent experimental data as depicted in Figure 2.1. Solid lines are from numerical simulations using the EGP model, parameters are listed in Appendix A.

As a starting point, the experimental data that was actually used to characterize the influence of deformation in the viscosity is evaluated, since these should naturally be captured well by the modifications. In Figure 5.5a, the response of simulations at different strain rates clearly shows the experimental data is well captured. Only at low strain rate, there is some overestimation of the stress at large deformation. This effect can be attributed to an excessive increase of the flow stress associated with the β process. however, this deviation could have been expected; when

inspecting Figure 5.3a more closely, it shows that at the maximum strain level the slope of the $(\alpha + \beta)$-process does not exactly match that of the experimental data. The compression tests at different temperatures (Figure 5.5b), are also well captured over the whole range of these temperatures. Thus, the model is capable of capturing both the experimentally observed rate dependence, as well as the experimentally observed temperature dependence in the strain hardening. Up to now, the EGP model was only capable of describing the large strain mechanical behavior at a single temperature. Therefore, this is indeed a considerable improvement of the model.

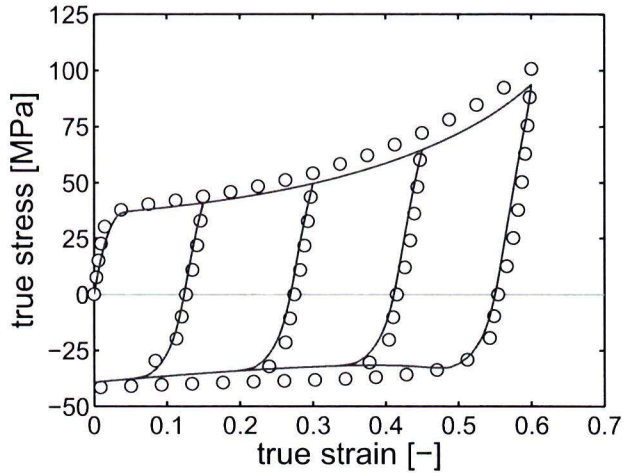

Figure 5.6: An impression of the mechanical response of PC in cyclic uniaxial deformation (symbols), as seen in Figure 5.1, compared to numerical simulations using the EGP model (solid lines), parameters are listed in Appendix A.

A more critical evaluation of the model performance is to check whether it is also capable of providing quantitative predictions of the orientation induced Bauschinger effect, as depicted in Figure 5.1. To check whether the observed behavior is indeed captured by the model, uniaxial tension/compression cycles are simulated using the same parameter set as in the previous paragraph, see Appendix A. As the specimens are mechanically rejuvenated, the effect of aging is canceled ($S_0 = 0$). The results in Figure 5.6 clearly show that the main features of the the experimental observations are qualitatively captured: after the loading direction is reversed at large strains, the subsequent compressive yield stress is considerably smaller than the momentary stress just before reversing the direction of deformation. However, a quantitative comparison shows that both in the tensile and the compressive stage of the deformation, the absolute stress is underestimated by the model. The first question that arises is whether the experimental data sets from Figure 5.5 and the one from Figure 5.6 are mutually consistent. Fortunately, there is an opportunity to check whether this is the case, since uniaxial compression data from the unoriented preconditioned tensile bars is available. The response from these compression tests can be directly compared to the response from compression tests at the same strain rate on non-preconditioned samples, i.e. Figure 5.5a. Figure 5.7a shows that at yield the difference in stress is extensive, which is of course obvious, as one sample is rejuvenated. In the strain hardening regime, however, the response should be the same. This is obviously not the case, as at large strains a stress difference remains of approximately 5 MPa. The cause for this deviation can only be the preconditioning, since this is the only difference between the two samples. As mentioned before, the preconditioning consists of applying large strain torsion to an axisymmetric tensile bar and subsequently twisting it back to its original position. During torsion, the axial direction should be stress free, but this is difficult to accomplish in practice due to the fact that this preconditioning was done on a lathe in the absence of testing equipment capable of reaching the desired torsion-angle. It is therefore not unlikely that during the twisting of the bar, a residual plastic strain was induced by (unintended)

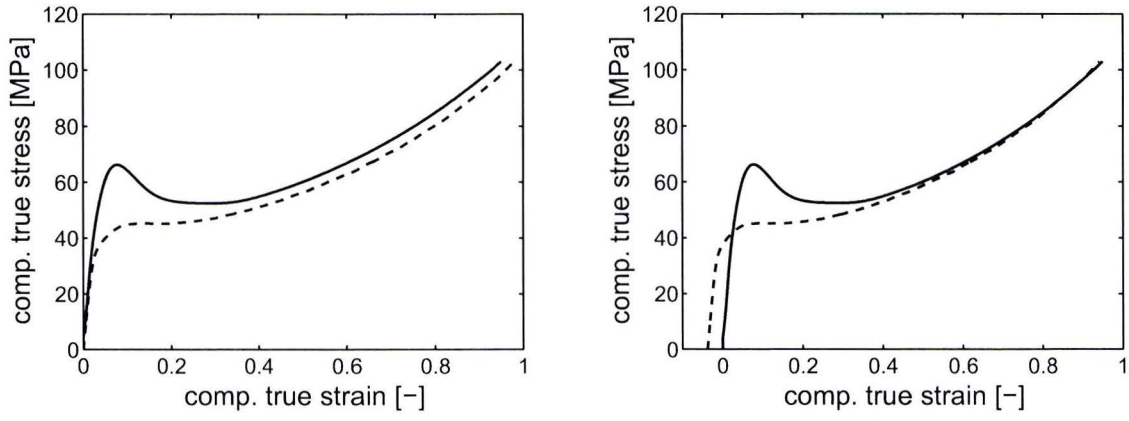

Figure 5.7: (a) Comparison of stress-strain response from an isotropic untreated specimen (solid line) and an unoriented mechanically preconditioned specimen (dashed line) of PC at a compressive strain rate of 10^{-4} s^{-1}. (b) Corrected for residual plastic strain in preconditioned specimen.

axial loading. Indeed, it is demonstrated in Figure 5.7b that assuming a small residual strain for the preconditioned specimen causes the large strain behavior of both tests to coincide. The effect observed is actually the reason for the aforementioned inconsistency of the elastic strain hardening parameters, compare Tables 4.1 and 5.1. Figure 5.8 demonstrates that when this offset

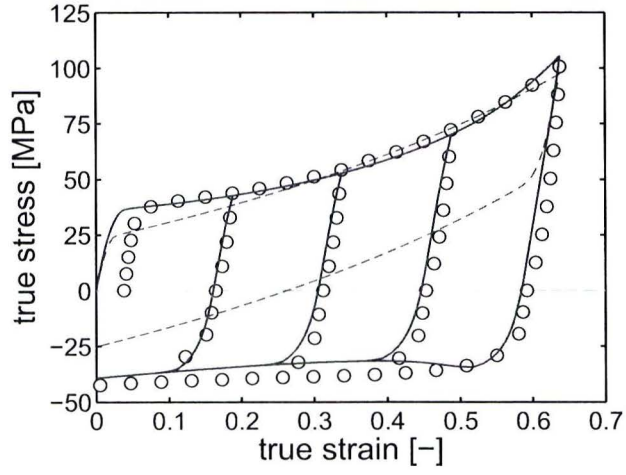

Figure 5.8: Experimental data (symbols) from Figure 5.6, adjusted by using Figure 5.7b, compared to numerical simulations(solid lines).

is accounted for in the experimental results, the cyclic deformation tests are accurately predicted by the model. This proves that the suggested modifications of the EGP model are a substantial improvement, since the original version of the EGP model is not able to capture the Bauschinger effect (see Figure 5.8, dashed line). Note that the modifications and characterizations of the model were done solely on the basis of the sets of compression data in Figure 5.5.

Chapter 6

Discussion

In the previous chapter, it was shown that the introduction of a viscous strain hardening contribution in the EGP model signifies a substantial improvement of its capability to quantitatively describe the mechanical response of PC under various conditions. However, there is a puzzling issue that remains to be addressed, namely the shift in the β-process that was observed by Senden *et al.* [24]. As discussed in Section 4.3, they used mechanically preconditioned specimens of PC for tensile testing at a constant strain rate up to a predefined strain level; after unloading, tensile tests were performed at varying strain rates. With this method, which will be referred to as *method A*, they characterized the change in yield kinetics with the deformation by plotting the tensile yield stresses from specimens with various levels of prestrain, as a function of strain rate, see Figure 6.1a. It was observed that, in the isotropic case ($\varepsilon_{pre} = 0$), the yield kinetics were well described with the α-process that is known to be present in PC. However, this changed already with remarkably small amounts of prestrain, as all the subsequent prestrain levels ($\varepsilon \geq 0.15$) contain a contribution from the β-process. This is shown by the solid lines, which are fits using the Ree-Eyring relation and the activation volumes that relate to the α- and β-process (Table 2.1). Therefore, it was concluded that the deformation induced change in slope was caused by a shift of the β-process towards lower strain rates. This is, of course, the exact same conclusion as was

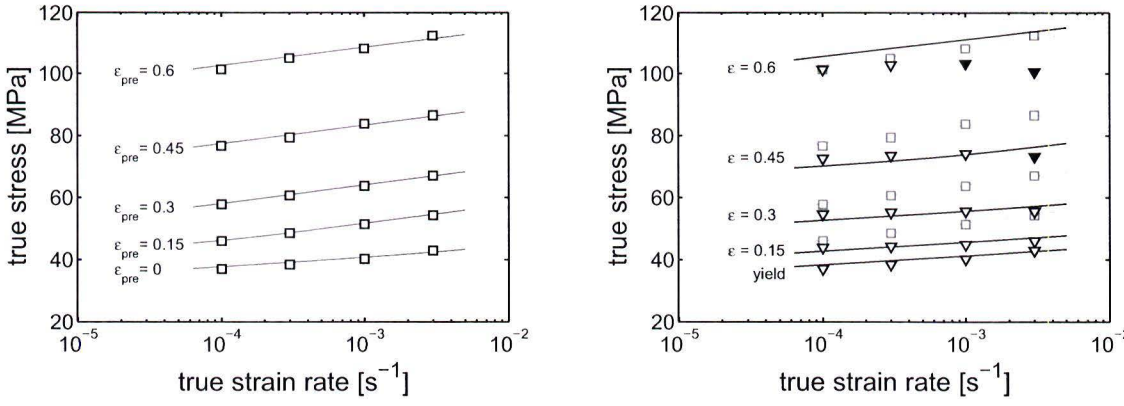

(a) (b)

Figure 6.1: (a) Tensile yield stress as a function of strain rate for oriented PC (square markers); various levels of true prestrain are indicated. Solid lines are fits using Equation (2.3). (b) Stress at various strain levels (as indicated) from uniaxial tensile tests on isotropic PC (triangular markers) and predictions from numerical simulations of the EGP model (solid lines). As a comparison, the data from (a) is added in grey; filled markers indicate that the data is obscured by viscous heating. Data taken from [24].

drawn in Chapter 3, the difference being the procedure applied to characterize the phenomenon (*method B*). What is striking, however, is the difference in the level of strain at which the β-process starts contributing to the stress: with method A it is already observed at a tensile strain of 0.15, while with method B it does not appear before a compressive strain of 0.5 (see Figure 3.2b).

In Figure 6.1b, the results are shown using method B, but now applied to the data used in method A. Or more precisely, as the isotropic preconditioned tensile bars from method A where tested well beyond yield for the different true strain rates, the stress response could be evaluated at various strain levels (triangular markers), i.e. method B. This figure clearly shows that there is indeed a discrepancy between the results from the two methods, as a completely different deformation-induced behavior is observed, compared to that in Figure 6.1a. Up to $\varepsilon = 0.45$, the slopes remain the same as the one observed at yield, while it even decreases at ($\varepsilon = 0.6$). The decrease in slope at this strain level, though, is caused by viscous heating of the sample; at high strain rates the heat generated in the sample exceeds the amount that can be transported to the surrounding, causing the sample temperature to increase with increasing deformation. The measured stress is therefore too low (filled markers) and it is omitted from the analysis. Results of numerical simulations, using the EGP model (solid lines) with the parameters from Appendix A, support the observation that the yield kinetics remain initially the same and shift to lower strain rates with deformation. As mentioned, the shift of the β-process is such that the contribution of this process only becomes visible at the highest strain depicted. Finally, it should be noted that the stresses using method B are determined at the measured levels of strain. The residual plastic strain (see Figure 5.7) is accounted for in the simulation results.

The question remains what causes the different observations that result from methods A and B. To this end, it should be recognized that the two methods only differ in one aspect: in the method A, used by Senden *et al.*, the sample is subjected to a intermittent loading path, as the load is removed between predeformation and the subsequent tensile test; whereas in method B, the load is never removed, as an ongoing tensile test is evaluated. That these different approaches lead to a different response, is illustrated in Figure 6.2a, where for a single strain rate the mechanical response of specimens with various levels of preorientation is plotted as a function of the total strain, i.e. including the prestrain of the sample It is clear that all collapse onto a single curve at large strains,

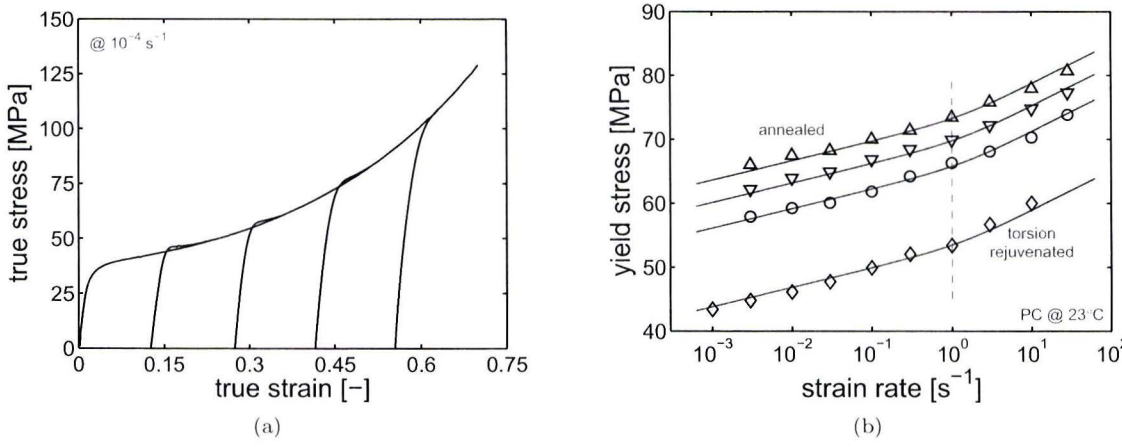

(a) (b)

Figure 6.2: (a) Mechanical response of preoriented PC in uniaxial tension, at a single strain rate, as a function of the total strain. Data taken from [24]. (b) Tensile yield stress of PC as a function of strain rate for different thermo-mechanical histories. Data taken from [8].

but more intriguing is the behavior of the prestrained samples at yield: a small amount of strain softening can be distinguished, especially in the samples with smaller preorientation. The yield

kinetics here are governed by the $(\alpha+\beta)$-process, which can be seen in Figure 6.1a, while the yield kinetics found by method B indicate a contribution from the α-process, as seen in Figure 6.1b. It is clear that the β-process becomes visible in method A due to the unloading and reloading prior to the tensile test, as this is the only difference with method B. It is known that at room temperature the β-process of PC is completely relaxed and in equilibrium, which leads to a constant contribution to stress, regardless of the thermo-mechanical history [1]. This is demonstrated in Figure 6.2b, where the deformation kinetics of PC are shown with four different levels of aging. It is clear that this affects the stress response in the α-process, whereas the β-contribution remains constant: the β-process shows at the exact same location when the sample is rejuvenated, compared to the ones that are annealed. Due to the high mobility of this process, the rejuvenation procedure has no effect on the experimental observations, as it (almost) instantaneously aged.

It appears that, due to the high mobility of the β-process, both physical aging and orientation have an important influence on the deformation-induced changes in the deformation kinetics. This can be understood when realizing that, from a modeling point of view, aging affects the initial viscosity (see Equation (4.12)) in a similar way as deformation does (see Equation (5.4)). The interplay between these mechanisms can be interpreted as follows. At the start of an uniaxial tensile test (A), as depicted in Figure 6.3b, the β-process lies outside the experimental time-scale,

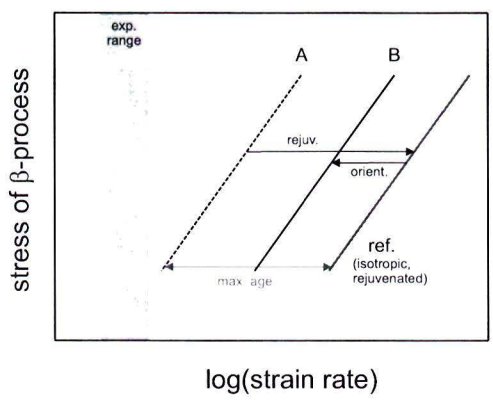

(a) A → B

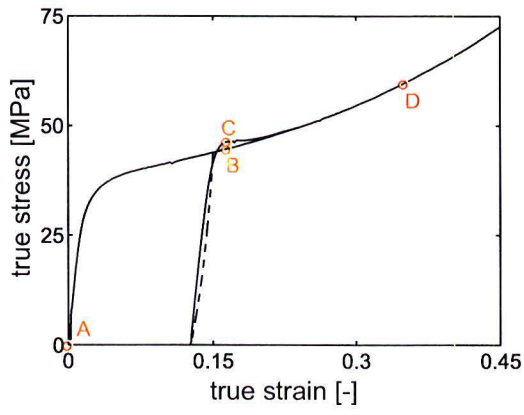

(b)

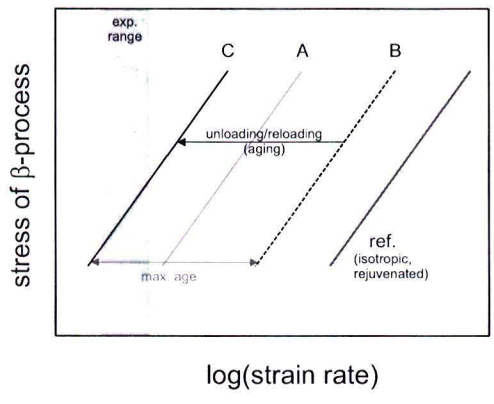

(c) B → C

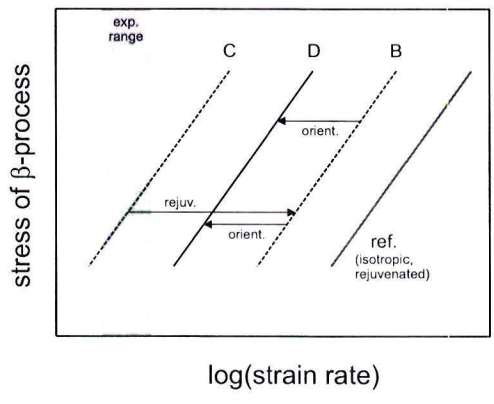

(d) B/C → D

Figure 6.3: Schematic representations of the shift in the β-process: (a) loading from (A) to (B), (c) unloading and subsequent reloading from (B) to (C), and (d) continuing the deformation from either (B) or (C) towards (D). The different stages are specified in (b).

see Figure 6.3a. Since it ages instantaneously, it is in its isotropic thermodynamic equilibrium state (i.e. fully aged) and thus possesses its maximum amount of aging, which is reflected by its distance from the reference state (*ref*). This reference state is the isotropic, rejuvenated state of the β-process.

When the material starts deforming towards (B), rejuvenation causes the β-process to shift towards higher strain rates, while the simultaneous orientation shows a opposite effect, as a result of the deformation dependence of the flow stress. At some point, the rejuvenation stops and only the second effect remains. Depending on its amount of deformation, (B) will lie at some position between (A) and the reference state (*ref*). Here B is chosen such that it is fully rejuvenated.

From Figure 6.3b it is clear that there are two ways to reach (D): directly from (B) by continuing the deformation, or after first unloading and the reloading via (C). The unloading and reloading process is illustrated in Figure 6.3c. Since the total strain at (B) and (C) is equal, the level of orientation at these points is also the same, implying that (B) and (C) share the same rejuvenated reference state. In fact, (B) is the rejuvenated reference state of (C), provided that the β contribution has fully rejuvenated in the deformation process from (A) to (B). The main difference between (B) and (C) is the thermodynamic state of the material. As mentioned, the β-process ages instantaneous in the unloading/reloading process, shifting it to the range of strain rates where it can be experimentally observed. For the sake of simplicity, in the schematic pictures of Figures 6.3a and 6.3c it is assumed that the 'maximum age' of the isotropic material is equal to that of the oriented material.

With ongoing deformation, the material always ends up in (D). The process of going to (D) from either (B) or (C) is illustrated in Figure 6.3d. Coming from (B) the mechanism is straightforward: as the β-process in (B) is already fully rejuvenated, the only change when going to (D) is due to orientation. Of course, the path from (C) to (D) is characterized by exactly the same effect of orientation. However, this path is also influenced by mechanical rejuvenation. When deformed even further, the rejuvenated reference state of the β-process eventually shifts into the experimentally accessible range of strain rates. When this happens, approximately at $\varepsilon \geq 0.5$, the two methods A and B that are used to characterize the deformation dependence of the deformation kinetics give the same result: the kinetics are in the $(\alpha + \beta)$ regime, see Figure 6.1b. The same can also be observed in Figure 6.2a, as the tensile curve of the sample with a prestrain of 0.6 shows no longer any softening; the effect is overwhelmed by the influence of the orientation. The conclusion that must be drawn from these results is that the stress-accelerated aging that occurs during unloading/reloading makes it much more difficult to isolate the influence of orientation on the deformation kinetics, since the effect is obscured by aging of the β-process.

This has a notable implication on the results that were presented in this work regarding the tension/compression cycle simulations that were discussed in Section 5.2. As mentioned, the specimens for the compression test were machined from a tensile bar that had been preoriented to a specific level of strain. This suggests that in the subsequent compression tests the β-process is actually contributing to the total stress, because it acquired its equilibrium state during the time between the preorientation and the compression test. When reviewing the results from the numerical simulations with the modified EGP model, see Figure 5.8, it is noticed that the stresses in compression are somewhat underestimated, apart from the compressive yield stress of the specimen preoriented to $\varepsilon = 0.6$. This observation may be explained by the fact that the accelerated aging effect in the β-process is not taken into account in the simulation, i.e. the β-process is assumed to be rejuvenated in these compression simulations and does not contribute to the stress for the low prestrains. As previously concluded, this is not an issue for the tests at a prestrain of 0.6, which explains the correct prediction of the compressive yield stress at this prestrain.

Chapter 7

Conclusion

The central goal of this study is to improve the performance of the EGP model by adding a viscous contribution to the strain hardening; of course, without losing its qualities. For this purpose, the evolution of the flow stress with deformation is investigated for polycarbonate, the model material in this study. It is found that the deformation dependence in the viscosity should be incorporated in two parameters for each process: the initial viscosity and the activation energy. The former follows from the observation that, in polycarbonate, although the stress increases with deformation, the slope when plotted as a function of strain rate remains constant for both processes as they shift towards lower strain rates; the latter results from the observation that, when plotting the stress as a function of temperature, the slope increases with increasing deformation.

The change with deformation of these parameters is characterized, and this deformation dependence is incorporated into the EGP model. Numerical simulations show that this still allows to describe the mechanical response of polycarbonate over a vast range of strain rates, but more significantly, it also enables to describe the mechanical response for various temperatures with a single set of parameters. Furthermore, it is shown that reversed loading is also captured by the model. These last two features form a significant improvement of the model, as neither were captured before.

Bibliography

[1] C. Bauwens-Crowet and J-C. Bauwens. Effect of thermal history on the tensile yield stress of polycarbonate in the β transition range. *Polymer*, 24(7):921–924, 1983.

[2] C. Bauwens-Crowet, J-C. Bauwens, and G. Homès. The temperature dependence of yield of polycarbonate in uniaxial compression and tensile tests. *Journal of Materials Science*, 7(2):176–183, 1972.

[3] M.C. Boyce and R.N. Haward. *The Physics of Glassy Polymers, 2nd ed.*, chapter 5, pages 213–293. Chapman & Hall, London, 1997.

[4] M.C. Boyce, D.M. Parks, and A.S. Argon. Large inelastic deformation of glassy polymers. part i: Rate dependent constitutive model. *Mechanics of materials*, 7:15–33, 1988.

[5] M.C. Boyce, G.G. Weber, and D.M. Parks. On the kinematics of finite strain plasticity. *Journal of the Mechanics and Physics of Solids*, 37(5):647–665, 1989.

[6] C.P. Buckley and D.C. Jones. Glass-rubber constitutive model for amorphous polymers near the glass transition. *Polymer*, 36(17):3301–3312, 1995.

[7] S.F. Edwards and Th. Vilgis. The effect of entanglements in rubber elasticity. *Polymer*, 27(4):483–492, 1986.

[8] T.A.P. Engels. *Predicting Performance of Glassy Polymers*. PhD thesis, Eindhoven University of Technology, Eindhoven, 2008.

[9] T.A.P. Engels, L.E. Govaert, and H.E.H. Meijer. The influence of molecular orientation on the yield and post-yield response of injection-molded polycarbonate. *Macromol. Mater. Eng.*, 294(12):821–828, 2009.

[10] H. Eyring. Viscosity, plasticity, and diffusion as examples of absolute reaction rates. *The Journal of Chemical Physics*, 4:283–291, 1936.

[11] L.E. Govaert, T.A.P. Engels, M. Wendlandt, T.A. Tervoort, and U.W. Suter. Does the strain hardening modulus of glassy polymers scale with the flow stress? *J. Polym. Sci., Part B: Polym. Phys.*, 46(22):2475–2481, 2008.

[12] L.E. Govaert and T.A. Tervoort. Strain hardening of polycarbonate in the glassy state: influence of temperature and molecular weight. *J. Polym. Sci., Polym.Phys.Ed.*, 42(11):2041–2049, 2004.

[13] L.E. Govaert, P.H.M. Timmermans, and W.A.M. Brekelmans. The influence of intrinsic strain softening on strain localization in polycarbonate: modeling and experimental validation. *J. Engng. Mat. Technol.*, 122:177–185, 2000.

[14] G.I. Gurevich and P.P. Kobeko. A study of polymers. iii. technique of mechanical tests of vulcanizates of rubber and plastics. *Rubber Chem. Technol.*, 13(4):904–917, 1940.

[15] R. N. Haward and G. Thackray. The use of a mathematical model to describe isothermal stress-strain curves in glassy thermoplastics. *Proc. R. Soc. Lond. A*, 302(1471):453–472, 1968.

[16] E.T.J. Klompen, T.A.P. Engels, L.E. Govaert, and H.E.H. Meijer. Modelling of the post-yield response of glassy polymers: influence of thermomechanical history. *Macromolecules*, 38(16):6997–7008, 2005.

[17] E.T.J. Klompen and L.E. Govaert. Nonlinear viscoelastic behaviour of thermorheologically complex materials: a modeling approach. *Mech. Time-depend. Mater.*, 3(1):49–69, 1999.

[18] E.J Kramer. Open questions in the physics of deformation of polymer glasses. *Journal of Polymer Science, Part B: Polymer Physics*, 43(23):3369–3371, 2005.

[19] H.X. Li and C.P. Buckley. Evolution of strain localization in glassy polymers: A numerical study. *International Journal of Solids and Structures*, 46(7-8):1607–1623, 2009.

[20] H.E.H. Meijer and L.E. Govaert. Mechanical performance of polymer systems: The relation between structure and properties. *Prog. Polym. Sci.*, 30(8):915–938, 2005.

[21] T. Ree and H. Eyring. Theory of non-newtonian flow. i. solid plastic system. *Journal of Applied Physics*, 26(7):793–800, 195.

[22] J.A. Roetling. Yield stress behavior of polymethylmethacrylate. *Polymer*, 6:311–317, 1965.

[23] D.J.A. Senden. Conference report, unpublished, 2010.

[24] D.J.A. Senden, J.A.W. van Dommelen, and L.E. Govaert. Strain hardening and its relation to bauschinger effects in oriented polymers. *J. Polym. Sci., Part B: Polym. Phys.*, 48(13):1483–1494, 2010.

[25] T.A. Tervoort and L.E. Govaert. Strain-hardening behavior of polycarbonate in the glassy state. *J. Rheol.*, 44(6):1263–1277, 2000.

[26] L.C.A. van Breemen. *Contact mechanics in glassy polymers*. PhD thesis, Eindhoven University of Technology, Eindhoven, 2009.

[27] L.C.A. van Breemen, E.T.J. Klompen, L.E. Govaert, and H.E.H. Meijer. Extending the egp constitutive model for polymer glasses to multiple relaxation times. *J. Mech. Phys. Solids*, 59:on line, 2011.

[28] M. Wendlandt, T.A. Tervoort, and U.W. Suter. Non-linear, rate-dependent strain-hardening behavior of polymer glasses. *Polymer*, 46:11786–11797, 2005.

Appendix A

Parameters EGP model

In Section 5.2 the intrinsic mechanical behavior of PC was characterized using a multi process version of the EGP model. The α-process was described with a relaxation spectrum consisting of 17 modes, as determined by Van Breemen *et al.* [27]. As this spectrum was determined for a single temperature, it has to be converted to the temperature-independent one. Furthermore, it is adapted to account for the higher initial viscosity needed, due to a different elastic strain hardening contribution, see Section 4.3. This results in the following:

$$\eta_{0,\alpha,i} = \eta_{0,\alpha,i,ref}(T) \cdot \exp\left(\frac{-\Delta U_{x,0}}{RT}\right) \cdot \exp(10.074). \tag{A.1}$$

Due to these changes, the shear moduli also needs correction: $G_{\alpha,i} = 0.9 \cdot G_{\alpha,i,ref}$. In Table A.1 the relaxation spectrum of the α-process is listed. The β-process is described by a single mode. Other parameters used are listed in Table A.2.

Table A.1: Relaxation spectrum for the α-process.

i	$G_{\alpha,i}$ [MPa]	$\eta_{0,\alpha,i}$ [MPa·s]
1	$3.17 \cdot 10^{2}$	$2.06 \cdot 10^{-28}$
2	$5.00 \cdot 10^{1}$	$3.42 \cdot 10^{-30}$
3	$4.03 \cdot 10^{1}$	$2.90 \cdot 10^{-31}$
4	$3.71 \cdot 10^{1}$	$2.79 \cdot 10^{-32}$
5	$3.15 \cdot 10^{1}$	$2.49 \cdot 10^{-33}$
6	$2.88 \cdot 10^{1}$	$2.40 \cdot 10^{-34}$
7	$2.48 \cdot 10^{1}$	$2.16 \cdot 10^{-35}$
8	$2.19 \cdot 10^{1}$	$2.00 \cdot 10^{-36}$
9	$1.86 \cdot 10^{1}$	$1.80 \cdot 10^{-37}$
10	$1.63 \cdot 10^{1}$	$1.65 \cdot 10^{-38}$
11	$1.39 \cdot 10^{1}$	$1.48 \cdot 10^{-39}$
12	$1.22 \cdot 10^{1}$	$1.38 \cdot 10^{-40}$
13	$1.07 \cdot 10^{1}$	$1.25 \cdot 10^{-41}$
14	$8.82 \cdot 10^{0}$	$1.08 \cdot 10^{-42}$
15	$9.36 \cdot 10^{0}$	$1.21 \cdot 10^{-43}$
16	$1.90 \cdot 10^{0}$	$2.57 \cdot 10^{-45}$
17	$1.48 \cdot 10^{1}$	$2.10 \cdot 10^{-45}$

Table A.2: Parameters describing PC, used in Section 5.2

x	G_x [MPa]	$\eta_{0,x}$ [MPa·s]	$C_{1,x}$ [-]	$\Delta U_{x,0}$ [kJ/mol·K]	$C_{2,x}$ [kJ/mol·K]	V_x^* [nm^3]	$S_{0,x}$ [-]	$r_{0,x}$ [-]	$r_{1,x}$ [-]	$r_{2,x}$ [-]	μ_x [-]
α	Table A.1	Table A.1	-22.0	245	73.7	5.32	17.5	0.965	50	-5	0.08
β	315	$4.0 \cdot 10^{-2}$	-11.0	50	36.3	5.06	0	0.965	50	-5	0.08

Appendix B

1-D stress from EGP model

Under the assumption that the material behaves incompressible, it is possible to derive a simple linear relationship between the stress and the logarithm of the constant strain rate.

For incompressible behavior the total stress $\boldsymbol{\sigma}$ can be described by:

$$\boldsymbol{\sigma} = -p\boldsymbol{I} + 2\eta_\alpha \boldsymbol{D}_{p,\alpha} + 2\eta_\beta \boldsymbol{D}_{p,\beta} + \boldsymbol{\sigma}_{r,e}, \tag{B.1}$$

where the unknown hydrostatic pressure p follows from the boundary conditions, the second term represents the flow contribution from the viscosity η (Equation (4.12)) and the last term represents the elastic contribution to strain hardening, which is described by the Edwards-Vilgis rubber-elastic model, see Section 4.3 and Appendix C. Because the entanglement network remains intact, the parameter representing the freedom of movement of the slip-links is zero. Now Equation (C.38) can be written as:

$$\boldsymbol{Z} = \frac{\alpha_*^2(1-\alpha_*^2)}{(1-\alpha_*^2 \mathrm{tr}\,(\boldsymbol{B}))^2}\mathrm{tr}\,(\boldsymbol{B})\,\boldsymbol{I} + \frac{1-\alpha_*^2}{1-\alpha_*^2\mathrm{tr}\,(\boldsymbol{B})}\boldsymbol{I} - \frac{\alpha_*^2}{1-\alpha_*^2\mathrm{tr}\,(\boldsymbol{B})}\boldsymbol{I}. \tag{B.2}$$

Combined with Equation (C.37),this leaves for the stress:

$$\boldsymbol{\sigma}_{r,e} = G_r\left[\frac{\alpha_*^2(1-\alpha_*^2)\mathrm{tr}(\boldsymbol{B})}{(1-\alpha_*^2\mathrm{tr}(\boldsymbol{B}))^2} + \frac{1-2\alpha_*^2}{1-\alpha_*^2\mathrm{tr}(\boldsymbol{B})}\right]\boldsymbol{B}^d. \tag{B.3}$$

For uniaxial deformation $\mathrm{tr}\,(\boldsymbol{B}) = (\lambda^2 + 2\lambda^{-1})$, where λ denotes the draw ratio, so the (1-D) stress response can be written as:

$$\begin{aligned}\sigma_{r,e} &= G_r\left[\frac{\alpha_*^2(1-\alpha_*^2)(\lambda^2+2\lambda^{-1})}{(1-\alpha_*^2(\lambda^2+2\lambda^{-1}))^2} + \frac{1-2\alpha_*^2}{1-\alpha_*^2(\lambda^2+2\lambda^{-1})}\right](\lambda^2-\lambda^{-1}) \\ &= G_r \cdot h(\lambda,\alpha_*).\end{aligned} \tag{B.4}$$

For uniaxial deformation under a constant strain rate, the resulting total stress σ and hydrostatic pressure p are (using $\dot{\gamma} = \sqrt{3}\dot{\varepsilon}$ and $\bar{\tau} = \sigma/\sqrt{3}$):

$$\sigma = 3\eta_\alpha \dot{\varepsilon}_{p,\alpha} + 3\eta_\beta \dot{\varepsilon}_{p,\beta} + G_r \cdot h(\lambda,\alpha_*) \qquad \text{and} \qquad p = -\tfrac{1}{3}\sigma, \tag{B.5}$$

where $\dot{\varepsilon}_{p,x}$ is the plastic strain rate of the process. It is assumed that:

- both processes have the same pressure dependence ($\mu = \mu_\alpha = \mu_\beta$),
- the material is fully rejuvenated ($S_x = 0$),
- the argument of the hyperbolic sine is large, and may therefore be approximated by an exponential function ($\sinh(x) \approx \frac{1}{2}\exp(x)$),

- the plastic strain rate of each process equals the applied *compressive* strain rate ($\dot{\varepsilon} = -\dot{\varepsilon}_{p,\alpha} = -\dot{\varepsilon}_{p,\beta}$).

For the viscosity (Equation (4.12)), these considerations leads to:

$$\eta_x = \frac{\tau_{0,x}}{\sqrt{3}\dot{\varepsilon}} \left[\ln\left(\frac{2\sqrt{3}\eta_{0,x}}{\tau_{0,x}} \dot{\varepsilon} \right) + \frac{\mu p}{\tau_{0,x}} + \frac{\Delta U_x}{RT} \right]. \tag{B.6}$$

Combining this with Equation (B.5) results in:

$$\sigma = \frac{-3}{\sqrt{3}-\mu} \sum_{x=\alpha,\beta} \tau_{0,x} \left[\ln\left(\frac{2\sqrt{3}\eta_{0,x}}{\tau_{0,x}} \dot{\varepsilon} \right) + \frac{\Delta U_x}{RT} \right] + \frac{\sqrt{3}}{\sqrt{3}-\mu} G_r \cdot h(\lambda, \alpha_*) \quad \text{with} \quad x = \alpha, \beta \tag{B.7}$$

Appendix C

Edwards-Vilgis theory

The part describing slip-links in the Edwards-Vilgis model [7] is given by:

$$W = \tfrac{1}{2} N_s kT \left[\frac{(1+\eta_*)(1-\alpha_*^2)}{1-\alpha_*^2 \sum_{i=1}^{3} \tilde{\lambda}_i^2} \sum_{i=1}^{3} \frac{\tilde{\lambda}_i^2}{1+\eta_* \tilde{\lambda}_i^2} + \sum_{i=1}^{3} \ln(1+\eta_* \tilde{\lambda}_i^2) + \ln\left(1-\alpha_*^2 \sum_{i=1}^{3} \tilde{\lambda}_i^2\right) \right], \quad \text{(C.1)}$$

where $\tilde{\lambda}_i$ (i = 1,2,3) are the principal stretch ratios, i.e. the eigenvalues of the isochoric left stretch tensor $\tilde{\boldsymbol{V}}$. The absolute temperature is denoted by T, Boltzmann's constant by k; the model parameters N_s, η_* and α_* represent the number density of slip links, the mobility of the slip links and the degree of inextensibility of the chains, respectively. The limit of $\eta_* = \alpha_* = 0$ corresponds to a neo-Hookean response. This expression can be rewritten in tensor notation as:

$$W = \frac{N_s\, k\, T}{2} \left[\frac{(1+\eta_*)(1-\alpha_*^2)}{1-\alpha_*^2 \operatorname{tr}\left(\tilde{\boldsymbol{B}}\right)} \operatorname{tr}\left(\tilde{\boldsymbol{B}} \cdot \left(\boldsymbol{I} + \eta_* \tilde{\boldsymbol{B}}\right)^{-1}\right) + \operatorname{tr}\left(\ln\left(\boldsymbol{I} + \eta_* \tilde{\boldsymbol{B}}\right)\right) + \ln\left(1-\alpha_*^2 \operatorname{tr}\left(\tilde{\boldsymbol{B}}\right)\right) \right], \quad \text{(C.2)}$$

where $\tilde{\boldsymbol{B}}$ is the isochoric Finger tensor. The equivalence of these two expressions for the free energy can be easily recognized when one realizes that the isochoric Finger tensor is symmetric and can therefore be written as:

$$\tilde{\boldsymbol{B}} = \tilde{\lambda}_1^2 \vec{n}_1 \vec{n}_1 + \tilde{\lambda}_2^2 \vec{n}_2 \vec{n}_2 + \tilde{\lambda}_3^2 \vec{n}_3 \vec{n}_3, \quad \text{(C.3)}$$

where the eigenvectors $\vec{n}_1$, $\vec{n}_2$ and $\vec{n}_3$ of $\tilde{\boldsymbol{B}}$ (or $\tilde{\boldsymbol{V}}$) form an orthogonal vector basis. In that case, the identity tensor is given by: $\boldsymbol{I} = \vec{n}_1 \vec{n}_1 + \vec{n}_2 \vec{n}_2 + \vec{n}_3 \vec{n}_3$. Naturally, Equation C.2 holds regardless of the vector basis that is used. A big advantage of this description, however, is that there is no need to calculate the eigenvalues and eigenvectors of the Finger tensor.

For the derivations that follow, it is more convenient to write Equation C.2 in a slightly different way:

$$W = \frac{N_s\, k\, T}{2} \left[\frac{(1+\eta_*)(1-\alpha_*^2)}{1-\alpha_*^2 \operatorname{tr}\left(\tilde{\boldsymbol{B}}\right)} \operatorname{tr}\left(\tilde{\boldsymbol{B}} \cdot \left(\boldsymbol{I} + \eta_* \tilde{\boldsymbol{B}}\right)^{-1}\right) + \ln\left(\det\left(\boldsymbol{I} + \eta_* \tilde{\boldsymbol{B}}\right)\right) + \ln\left(1-\alpha_*^2 \operatorname{tr}\left(\tilde{\boldsymbol{B}}\right)\right) \right], \quad \text{(C.4)}$$

where use has been made of the tensor rule: $\operatorname{tr}(\boldsymbol{A}) = \ln(\det(\exp(\boldsymbol{A})))$. Also, it is easily verified that the free energy function is invariant to rigid-body rotations. Here, this is proven solely for the only non-trivial term:

$$
\begin{aligned}
a &= \mathrm{tr}\left(\tilde{\boldsymbol{B}} \cdot \left(\boldsymbol{I} + \eta_* \tilde{\boldsymbol{B}}\right)^{-1}\right) \\
a^* &= \mathrm{tr}\left(\boldsymbol{Q} \cdot \tilde{\boldsymbol{B}} \cdot \boldsymbol{Q}^T \cdot \left(\boldsymbol{Q} \cdot \boldsymbol{I} \cdot \boldsymbol{Q}^T + \eta_* \boldsymbol{Q} \cdot \tilde{\boldsymbol{B}} \cdot \boldsymbol{Q}^T\right)^{-1}\right) \\
&= \mathrm{tr}\left(\boldsymbol{Q} \cdot \tilde{\boldsymbol{B}} \cdot \boldsymbol{Q}^T \cdot \left(\boldsymbol{Q} \cdot \left(\boldsymbol{I} + \eta_* \tilde{\boldsymbol{B}}\right) \cdot \boldsymbol{Q}^T\right)^{-1}\right) \\
&= \mathrm{tr}\left(\boldsymbol{Q} \cdot \tilde{\boldsymbol{B}} \cdot \boldsymbol{Q}^T \cdot \boldsymbol{Q}^{-T} \cdot \left(\boldsymbol{I} + \eta_* \tilde{\boldsymbol{B}}\right)^{-1} \cdot \boldsymbol{Q}^{-1}\right) \\
&= \mathrm{tr}\left(\boldsymbol{Q} \cdot \tilde{\boldsymbol{B}} \cdot \left(\boldsymbol{I} + \eta_* \tilde{\boldsymbol{B}}\right)^{-1} \cdot \boldsymbol{Q}^{-1}\right) \\
&= \mathrm{tr}\left(\tilde{\boldsymbol{B}} \cdot \left(\boldsymbol{I} + \eta_* \tilde{\boldsymbol{B}}\right)^{-1}\right) \\
&= a.
\end{aligned} \tag{C.5}
$$

Because of its invariance to rotations, the expression for W can also be written in terms of the isochoric right Cauchy Green deformation tensor, which is easier for the derivations that follow:

$$
W = \frac{N_s\, k\, T}{2}\left[\frac{(1+\eta_*)(1-\alpha_*^2)}{1-\alpha_*^2\,\mathrm{tr}\left(\tilde{\boldsymbol{C}}\right)}\,\mathrm{tr}\left(\tilde{\boldsymbol{C}} \cdot \left(\boldsymbol{I} + \eta_* \tilde{\boldsymbol{C}}\right)^{-1}\right) + \ln\left(\det\left(\boldsymbol{I} + \eta_* \tilde{\boldsymbol{C}}\right)\right) + \ln\left(1 - \alpha_*^2\,\mathrm{tr}\left(\tilde{\boldsymbol{C}}\right)\right)\right]. \tag{C.6}
$$

Intermezzo 1: tensor algebra

First, the applied definition of the derivative of a second-order tensor to another second-order tensor is given:

$$
\frac{\partial \boldsymbol{A}}{\partial \boldsymbol{B}} = \frac{\partial A_{ij}}{\partial B_{mn}} \vec{e}_i \vec{e}_j \vec{e}_n \vec{e}_m. \tag{C.7}
$$

Then, in case of a second-order tensor the chain rule can be applied as:

$$
\frac{\partial \boldsymbol{A}}{\partial \boldsymbol{B}} : \frac{\partial \boldsymbol{B}}{\partial \boldsymbol{C}} = \frac{\partial A_{ij}}{\partial B_{mn}} \vec{e}_i \vec{e}_j \vec{e}_n \vec{e}_m : \frac{\partial B_{kl}}{\partial C_{op}} \vec{e}_k \vec{e}_l \vec{e}_p \vec{e}_o = \frac{\partial A_{ij}}{\partial B_{mn}} \frac{\partial B_{mn}}{\partial C_{op}} \vec{e}_i \vec{e}_j \vec{e}_p \vec{e}_o = \frac{\partial A_{ij}}{\partial C_{op}} \vec{e}_i \vec{e}_j \vec{e}_p \vec{e}_o = \frac{\partial \boldsymbol{A}}{\partial \boldsymbol{C}} \tag{C.8}
$$

Using this tensor derivative definition, the derivative of a second-order tensor with respect to itself can be written as:

$$
\frac{\partial \boldsymbol{A}}{\partial \boldsymbol{A}} = \frac{\partial A_{ij}}{\partial A_{mn}} \vec{e}_i \vec{e}_j \vec{e}_n \vec{e}_m = \delta_{im}\delta_{jn} \vec{e}_i \vec{e}_j \vec{e}_n \vec{e}_m = {}^4\boldsymbol{I}. \tag{C.9}
$$

And the derivative of the trace of a second-order tensor to the tensor itself as:

$$
\frac{\partial\,\mathrm{tr}\,(\boldsymbol{A})}{\partial \boldsymbol{A}} = \frac{\partial A_{ii}}{\partial A_{mn}} \vec{e}_n \vec{e}_m = \delta_{im}\delta_{in} \vec{e}_n \vec{e}_m = \delta_{nm} \vec{e}_n \vec{e}_m = \boldsymbol{I} \tag{C.10}
$$

The derivative of the inverse $\boldsymbol{A}^{-1}$ of a second-order tensor $\boldsymbol{A}$ with respect to the tensor itself can be determined by:

$$
\begin{aligned}
\frac{\partial \boldsymbol{I}}{\partial \boldsymbol{A}} &= \frac{\partial\left(\boldsymbol{A} \cdot \boldsymbol{A}^{-1}\right)}{\partial \boldsymbol{A}} \\
{}^4\boldsymbol{0} &= \frac{\partial \boldsymbol{A}}{\partial \boldsymbol{A}} \cdot \boldsymbol{A}^{-1} + \boldsymbol{A} \cdot \frac{\partial \boldsymbol{A}^{-1}}{\partial \boldsymbol{A}},
\end{aligned} \tag{C.11}
$$

which leads to:

$$\begin{aligned}\frac{\partial \boldsymbol{A}^{-1}}{\partial \boldsymbol{A}} &= -\boldsymbol{A}^{-1} \cdot \frac{\partial \boldsymbol{A}}{\partial \boldsymbol{A}} \cdot \boldsymbol{A}^{-1} \\ &= -\boldsymbol{A}^{-1} \cdot {}^{4}\boldsymbol{I} \cdot \boldsymbol{A}^{-1}. \end{aligned} \tag{C.12}$$

Intermezzo 2: hyperelasticity

From the conformational free energy (i.e. stored-energy function or strain energy density function), the (rubber-elastic) Cauchy stress response is derived as follows:

$$\boldsymbol{\sigma} = \frac{2}{J}\, \boldsymbol{F} \cdot \frac{\partial W}{\partial \boldsymbol{C}} \cdot \boldsymbol{F}^{T}. \tag{C.13}$$

Because the Edwards Vilgis conformational free energy only depends on the deformation through $\tilde{\boldsymbol{C}}$, the derivative can be written as:

$$\frac{\partial W}{\partial \boldsymbol{C}} = \frac{\partial W}{\partial \tilde{\boldsymbol{C}}} : \left(\frac{\partial \tilde{\boldsymbol{C}}}{\partial \boldsymbol{C}} + \frac{\partial \tilde{\boldsymbol{C}}}{\partial I_3} \frac{\partial I_3}{\partial \boldsymbol{C}} \right), \tag{C.14}$$

where $I_3 = \det(\boldsymbol{C}) = J^2$. The isochoric right Cauchy Green deformation tensor can be written as:

$$\tilde{\boldsymbol{C}} = J^{-2/3}\boldsymbol{C} = \sqrt{\det(\boldsymbol{C})}^{-2/3}\boldsymbol{C} = I_3^{-1/3}\boldsymbol{C}. \tag{C.15}$$

Now, the following partial derivatives can be calculated:

$$\frac{\partial \tilde{\boldsymbol{C}}}{\partial \boldsymbol{C}} = I_3^{-1/3}\, {}^{4}\boldsymbol{I}, \tag{C.16}$$

$$\frac{\partial \tilde{\boldsymbol{C}}}{\partial I_3} = -\frac{1}{3}\, I_3^{-4/3}\boldsymbol{C}, \tag{C.17}$$

$$\frac{\partial I_3}{\partial \boldsymbol{C}} = I_2\boldsymbol{I} - I_1\boldsymbol{C} + \boldsymbol{C}^2 = I_3\boldsymbol{C}^{-1}. \tag{C.18}$$

The last partial derivative was obtained using the Cayley-Hamilton theorem:

$$\boldsymbol{C}^3 - I_1\boldsymbol{C}^2 + I_2\boldsymbol{C} - I_3\boldsymbol{I} = \boldsymbol{0} \tag{C.19}$$

$$\boldsymbol{C}^2 - I_1\boldsymbol{C} + I_2\boldsymbol{I} - I_3\boldsymbol{C}^{-1} = \boldsymbol{0} \tag{C.20}$$

$$\boldsymbol{C}^2 - I_1\boldsymbol{C} + I_2\boldsymbol{I} = I_3\boldsymbol{C}^{-1}. \tag{C.21}$$

Substitution of these partial derivatives in Equation C.14 leads to:

$$\begin{aligned}\frac{\partial W}{\partial \boldsymbol{C}} &= \frac{\partial W}{\partial \tilde{\boldsymbol{C}}} : \left(I_3^{-1/3}\, {}^{4}\boldsymbol{I} - \frac{1}{3}\, I_3^{-4/3}\boldsymbol{C} I_3 \boldsymbol{C}^{-1} \right) \\ &= I_3^{-1/3} \left(\frac{\partial W}{\partial \tilde{\boldsymbol{C}}} - \frac{1}{3}\, \frac{\partial W}{\partial \tilde{\boldsymbol{C}}} : \boldsymbol{C}\boldsymbol{C}^{-1} \right). \end{aligned} \tag{C.22}$$

Finally, this relation can be substituted into Equation C.13, yielding:

$$
\begin{aligned}
\boldsymbol{\sigma} &= \frac{2}{J}\,\boldsymbol{F}\cdot I_3^{-1/3}\left(\frac{\partial W}{\partial \tilde{\boldsymbol{C}}} - \frac{1}{3}\,\frac{\partial W}{\partial \tilde{\boldsymbol{C}}} : \boldsymbol{C}\boldsymbol{C}^{-1}\right)\cdot \boldsymbol{F}^T \\
&= \frac{2}{J}\,I_3^{-1/3}\left(\boldsymbol{F}\cdot\frac{\partial W}{\partial \tilde{\boldsymbol{C}}}\cdot\boldsymbol{F}^T - \frac{1}{3}\,\boldsymbol{F}\cdot\left(\frac{\partial W}{\partial \tilde{\boldsymbol{C}}} : \boldsymbol{C}\right)\boldsymbol{C}^{-1}\cdot\boldsymbol{F}^T\right) \\
&= \frac{2}{J}\,J^{-2/3}\left(\boldsymbol{F}\cdot\frac{\partial W}{\partial \tilde{\boldsymbol{C}}}\cdot\boldsymbol{F}^T - \frac{1}{3}\,\frac{\partial W}{\partial \tilde{\boldsymbol{C}}} : \boldsymbol{C}\boldsymbol{I}\right) \\
&= \frac{2}{J}\left(\tilde{\boldsymbol{F}}\cdot\frac{\partial W}{\partial \tilde{\boldsymbol{C}}}\cdot\tilde{\boldsymbol{F}}^T - \frac{1}{3}\,\frac{\partial W}{\partial \tilde{\boldsymbol{C}}} : \tilde{\boldsymbol{C}}\boldsymbol{I}\right) \\
&= \frac{2}{J}\left(\tilde{\boldsymbol{F}}\cdot\frac{\partial W}{\partial \tilde{\boldsymbol{C}}}\cdot\tilde{\boldsymbol{F}}^T - \frac{1}{3}\,\mathrm{tr}\left(\frac{\partial W}{\partial \tilde{\boldsymbol{C}}}\cdot\tilde{\boldsymbol{C}}\right)\boldsymbol{I}\right) \\
&= \frac{2}{J}\left(\tilde{\boldsymbol{F}}\cdot\frac{\partial W}{\partial \tilde{\boldsymbol{C}}}\cdot\tilde{\boldsymbol{F}}^T\right)^d .
\end{aligned}
\tag{C.23}
$$

The validity of the last two steps in this derivation may not be evident and will be discussed next. Let the spectral decompositions of the isochoric right and left Cauchy Green deformation tensors be given by:

$$
\tilde{\boldsymbol{C}} = \sum_{i=1}^{3} \tilde{\lambda}_i^2 \vec{n}_{0_i}\vec{n}_{0_i} \qquad ; \qquad \tilde{\boldsymbol{B}} = \sum_{i=1}^{3} \tilde{\lambda}_i^2 \vec{n}_i\vec{n}_i, \tag{C.24}
$$

where the eigenvalues of both tensors, i.e. the isochoric principal stretches $\tilde{\lambda}_i$, are of course the same. The eigenvectors of both tensors differ by a rotation; the principal stretch directions $\vec{n}_{0_i}$ correspond to the reference state of the material, while $\vec{n}_i$ correspond to the deformed (current) state. Now, the deformation gradient tensor can also be written in terms of these quantities:

$$
\tilde{\boldsymbol{F}} = \sum_{i=1}^{3} \tilde{\lambda}_i \vec{n}_i\vec{n}_{0_i}. \tag{C.25}
$$

In addition to this, the derivative $\frac{\partial W}{\partial \tilde{\boldsymbol{C}}}$ can also be written in this way:

$$
\frac{\partial W}{\partial \tilde{\boldsymbol{C}}} = \sum_{i=1}^{3} a_{c_i}\vec{n}_{0_i}\vec{n}_{0_i}. \tag{C.26}
$$

The trace of the second order tensor $\tilde{\boldsymbol{F}}\cdot\frac{\partial W}{\partial \tilde{\boldsymbol{C}}}\cdot\tilde{\boldsymbol{F}}^T$ can now be elaborated:

$$
\begin{aligned}
\mathrm{tr}\left(\tilde{\boldsymbol{F}}\cdot\frac{\partial W}{\partial \tilde{\boldsymbol{C}}}\cdot\tilde{\boldsymbol{F}}^T\right) &= \mathrm{tr}\left(\sum_{i=1}^{3}\tilde{\lambda}_i\vec{n}_i\vec{n}_{0_i}\cdot\sum_{i=1}^{3}a_{c_i}\vec{n}_{0_i}\vec{n}_{0_i}\cdot\sum_{i=1}^{3}\tilde{\lambda}_i\vec{n}_{0_i}\vec{n}_i\right) \\
&= \mathrm{tr}\left(\sum_{i=1}^{3}a_{c_i}\tilde{\lambda}_i^2\vec{n}_i\vec{n}_i\right) \\
&= \mathrm{tr}\left(\sum_{i=1}^{3}a_{c_i}\tilde{\lambda}_i^2\vec{n}_{0_i}\vec{n}_{0_i}\right) \\
&= \mathrm{tr}\left(\frac{\partial W}{\partial \tilde{\boldsymbol{C}}}\cdot\tilde{\boldsymbol{C}}\right),
\end{aligned}
\tag{C.27}
$$

thus proving that the above derived Cauchy stress tensor is indeed deviatoric.

Derivative of the conformational free energy

As stated in Equation C.6, the conformational free energy can be expressed as:

$$W = \frac{N_s\, k\, T}{2}\left[\frac{(1+\eta_*)(1-\alpha_*^2)}{1-\alpha_*^2\,\mathrm{tr}\left(\tilde{\boldsymbol{C}}\right)}\,\mathrm{tr}\left(\tilde{\boldsymbol{C}}\cdot\left(\boldsymbol{I}+\eta_*\,\tilde{\boldsymbol{C}}\right)^{-1}\right)+\ln\left(\det\left(\boldsymbol{I}+\eta_*\,\tilde{\boldsymbol{C}}\right)\right)+\ln\left(1-\alpha_*^2\,\mathrm{tr}\left(\tilde{\boldsymbol{C}}\right)\right)\right]. \tag{C.28}$$

The derivative of this expression with respect to $\tilde{\boldsymbol{C}}$ is now determined step by step. As shown in the first intermezzo, the derivative of the trace of a tensor to the tensor itself can be written as:

$$\frac{\partial\,\mathrm{tr}\left(\tilde{\boldsymbol{C}}\right)}{\partial\tilde{\boldsymbol{C}}} = \boldsymbol{I}. \tag{C.29}$$

The next part of the derivative that is treated, is:

$$\begin{aligned}
\Rightarrow\quad & \frac{\partial\,\mathrm{tr}\left(\tilde{\boldsymbol{C}}\cdot\left(\boldsymbol{I}+\eta_*\,\tilde{\boldsymbol{C}}\right)^{-1}\right)}{\partial\tilde{\boldsymbol{C}}}\\
= \quad & \frac{\partial\,\mathrm{tr}\left(\tilde{\boldsymbol{C}}\cdot\left(\boldsymbol{I}+\eta_*\,\tilde{\boldsymbol{C}}\right)^{-1}\right)}{\partial\left(\tilde{\boldsymbol{C}}\cdot\left(\boldsymbol{I}+\eta_*\,\tilde{\boldsymbol{C}}\right)^{-1}\right)} : \left[\frac{\partial\tilde{\boldsymbol{C}}}{\partial\tilde{\boldsymbol{C}}}\cdot\left(\boldsymbol{I}+\eta_*\,\tilde{\boldsymbol{C}}\right)^{-1}+\tilde{\boldsymbol{C}}\cdot\left(\frac{\partial\left(\boldsymbol{I}+\eta_*\,\tilde{\boldsymbol{C}}\right)^{-1}}{\partial\left(\boldsymbol{I}+\eta_*\,\tilde{\boldsymbol{C}}\right)} : \frac{\partial\left(\boldsymbol{I}+\eta_*\,\tilde{\boldsymbol{C}}\right)}{\partial\tilde{\boldsymbol{C}}}\right)\right]\\
= \quad & \boldsymbol{I} : \left[{}^4\boldsymbol{I}\cdot\left(\boldsymbol{I}+\eta_*\,\tilde{\boldsymbol{C}}\right)^{-1}-\tilde{\boldsymbol{C}}\cdot\left(\left(\left(\boldsymbol{I}+\eta_*\,\tilde{\boldsymbol{C}}\right)^{-1}\cdot{}^4\boldsymbol{I}\cdot\left(\boldsymbol{I}+\eta_*\,\tilde{\boldsymbol{C}}\right)^{-1}\right) : \eta_*\,{}^4\boldsymbol{I}\right)\right]\\
= \quad & \boldsymbol{I} : {}^4\boldsymbol{I}\cdot\left(\boldsymbol{I}+\eta_*\,\tilde{\boldsymbol{C}}\right)^{-1}-\eta_*\,\boldsymbol{I} : \left(\tilde{\boldsymbol{C}}\cdot\left(\boldsymbol{I}+\eta_*\,\tilde{\boldsymbol{C}}\right)^{-1}\cdot{}^4\boldsymbol{I}\cdot\left(\boldsymbol{I}+\eta_*\,\tilde{\boldsymbol{C}}\right)^{-1}\right)\\
= \quad & \boldsymbol{I}\cdot\left(\boldsymbol{I}+\eta_*\,\tilde{\boldsymbol{C}}\right)^{-1}-\eta_*\,\left(\boldsymbol{I}\cdot\tilde{\boldsymbol{C}}\right) : \left(\left(\boldsymbol{I}+\eta_*\,\tilde{\boldsymbol{C}}\right)^{-1}\cdot{}^4\boldsymbol{I}\cdot\left(\boldsymbol{I}+\eta_*\,\tilde{\boldsymbol{C}}\right)^{-1}\right)\\
= \quad & \left(\boldsymbol{I}+\eta_*\,\tilde{\boldsymbol{C}}\right)^{-1}-\eta_*\,\tilde{\boldsymbol{C}} : \left(\left(\boldsymbol{I}+\eta_*\,\tilde{\boldsymbol{C}}\right)^{-1}\cdot{}^4\boldsymbol{I}\cdot\left(\boldsymbol{I}+\eta_*\,\tilde{\boldsymbol{C}}\right)^{-1}\right)\\
= \quad & \left(\boldsymbol{I}+\eta_*\,\tilde{\boldsymbol{C}}\right)^{-1}-\eta_*\,\left(\tilde{\boldsymbol{C}}\cdot\left(\boldsymbol{I}+\eta_*\,\tilde{\boldsymbol{C}}\right)^{-1}\right) : {}^4\boldsymbol{I}\cdot\left(\boldsymbol{I}+\eta_*\,\tilde{\boldsymbol{C}}\right)^{-1}\\
= \quad & \left(\boldsymbol{I}+\eta_*\,\tilde{\boldsymbol{C}}\right)^{-1}-\eta_*\,\tilde{\boldsymbol{C}}\cdot\left(\boldsymbol{I}+\eta_*\,\tilde{\boldsymbol{C}}\right)^{-1}\cdot\left(\boldsymbol{I}+\eta_*\,\tilde{\boldsymbol{C}}\right)^{-1}.
\end{aligned} \tag{C.30}$$

The next part of the derivative to be considered is:

$$\begin{aligned}
\Rightarrow\quad & \frac{\partial\,\ln\left(\det\left(\boldsymbol{I}+\eta_*\,\tilde{\boldsymbol{C}}\right)\right)}{\partial\tilde{\boldsymbol{C}}}\\
= \quad & \frac{\partial\,\ln\left(\det\left(\boldsymbol{I}+\eta_*\,\tilde{\boldsymbol{C}}\right)\right)}{\partial\det\left(\boldsymbol{I}+\eta_*\,\tilde{\boldsymbol{C}}\right)}\,\frac{\partial\,\det\left(\boldsymbol{I}+\eta_*\,\tilde{\boldsymbol{C}}\right)}{\partial\left(\boldsymbol{I}+\eta_*\,\tilde{\boldsymbol{C}}\right)} : \frac{\partial\left(\boldsymbol{I}+\eta_*\,\tilde{\boldsymbol{C}}\right)}{\partial\tilde{\boldsymbol{C}}}\\
= \quad & \frac{1}{\det\left(\boldsymbol{I}+\eta_*\,\tilde{\boldsymbol{C}}\right)}\,\det\left(\boldsymbol{I}+\eta_*\,\tilde{\boldsymbol{C}}\right)\left(\boldsymbol{I}+\eta_*\,\tilde{\boldsymbol{C}}\right)^{-T} : \eta_*\,\frac{\partial\tilde{\boldsymbol{C}}}{\partial\tilde{\boldsymbol{C}}}\\
= \quad & \left(\boldsymbol{I}+\eta_*\,\tilde{\boldsymbol{C}}\right)^{-1} : \eta_*\,{}^4\boldsymbol{I}\\
= \quad & \eta_*\,\left(\boldsymbol{I}+\eta_*\,\tilde{\boldsymbol{C}}\right)^{-1},
\end{aligned} \tag{C.31}$$

where use has been made of the fact that the derivative of the determinant $\det(\boldsymbol{A})$ of a second-order tensor $\boldsymbol{A}$ with respect to that tensor is equal to $\det(\boldsymbol{A})\boldsymbol{A}^{-T}$. The last part of the derivative to be considered is:

$$\begin{aligned}
\Rightarrow & \quad \frac{\partial \ln\left(1-\alpha_*^2 \operatorname{tr}\left(\tilde{\boldsymbol{C}}\right)\right)}{\partial \tilde{\boldsymbol{C}}} \\
= & \quad \frac{\partial \ln\left(1-\alpha_*^2 \operatorname{tr}\left(\tilde{\boldsymbol{C}}\right)\right)}{\partial\left(1-\alpha_*^2 \operatorname{tr}\left(\tilde{\boldsymbol{C}}\right)\right)} \frac{\partial\left(1-\alpha_*^2 \operatorname{tr}\left(\tilde{\boldsymbol{C}}\right)\right)}{\partial \operatorname{tr}\left(\tilde{\boldsymbol{C}}\right)} \frac{\partial \operatorname{tr}\left(\tilde{\boldsymbol{C}}\right)}{\partial \tilde{\boldsymbol{C}}} \\
= & \quad -\frac{\alpha_*^2}{1-\alpha_*^2 \operatorname{tr}\left(\tilde{\boldsymbol{C}}\right)} \boldsymbol{I}.
\end{aligned} \tag{C.32}$$

Putting all elements together, the desired expression for the derivative is obtained:

$$\begin{aligned}
\frac{2}{N_s\, k\, T} \frac{\partial W}{\partial \tilde{\boldsymbol{C}}} = & \quad \frac{\alpha_*^2(1+\eta_*)(1-\alpha_*^2)\boldsymbol{I}}{\left(1-\alpha_*^2 \operatorname{tr}\left(\tilde{\boldsymbol{C}}\right)\right)^2} \operatorname{tr}\left(\tilde{\boldsymbol{C}} \cdot \left(\boldsymbol{I}+\eta_* \tilde{\boldsymbol{C}}\right)^{-1}\right) \\
& + \frac{(1+\eta_*)(1-\alpha_*^2)}{1-\alpha_*^2 \operatorname{tr}\left(\tilde{\boldsymbol{C}}\right)} \left(\left(\boldsymbol{I}+\eta_* \tilde{\boldsymbol{C}}\right)^{-1} - \eta_* \tilde{\boldsymbol{C}} \cdot \left(\boldsymbol{I}+\eta_* \tilde{\boldsymbol{C}}\right)^{-1} \cdot \left(\boldsymbol{I}+\eta_* \tilde{\boldsymbol{C}}\right)^{-1}\right) \\
& + \eta_* \left(\boldsymbol{I}+\eta_* \tilde{\boldsymbol{C}}\right)^{-1} - \frac{\alpha_*^2}{1-\alpha_*^2 \operatorname{tr}\left(\tilde{\boldsymbol{C}}\right)} \boldsymbol{I}.
\end{aligned} \tag{C.33}$$

Calculating the Cauchy stress response

Using the relations introduced in previous sections, the Cauchy stress can simply be obtained by substituting Equation C.33 into Equation C.23, leading to a number of tensor multiplications that are first elaborated, before considering the entire expression for the stress. Using Equation C.24, one of the terms that appear in Equation C.33 can be written in terms of its principal values:

$$\left(\boldsymbol{I}+\eta_* \tilde{\boldsymbol{C}}\right)^{-1} = \sum_{i=1}^{3} \frac{1}{1+\eta_* \tilde{\lambda}_i^2} \vec{n}_{0_i} \vec{n}_{0_i}. \tag{C.34}$$

Now, one of the terms that will appear in the Cauchy stress expression can be rewritten (making use of Equations C.24 and C.25):

$$\begin{aligned}
\Rightarrow & \quad \tilde{\boldsymbol{F}} \cdot \left(\boldsymbol{I}+\eta_* \tilde{\boldsymbol{C}}\right)^{-1} \cdot \tilde{\boldsymbol{F}}^T \\
= & \quad \sum_{i=1}^{3} \tilde{\lambda}_i \vec{n}_i \vec{n}_{0_i} \cdot \sum_{i=1}^{3} \frac{1}{1+\eta_* \tilde{\lambda}_i^2} \vec{n}_{0_i} \vec{n}_{0_i} \cdot \sum_{i=1}^{3} \tilde{\lambda}_i \vec{n}_{0_i} \vec{n}_i \\
= & \quad \sum_{i=1}^{3} \frac{\tilde{\lambda}_i^2}{1+\eta_* \tilde{\lambda}_i^2} \vec{n}_i \vec{n}_i \\
= & \quad \tilde{\boldsymbol{B}} \cdot \left(\boldsymbol{I}+\eta_* \tilde{\boldsymbol{B}}\right)^{-1},
\end{aligned} \tag{C.35}$$

and a second one:

$$
\begin{aligned}
\Rightarrow \quad & \tilde{\boldsymbol{F}} \cdot \left(\tilde{\boldsymbol{C}} \cdot \left(\boldsymbol{I} + \eta_* \, \tilde{\boldsymbol{C}} \right)^{-1} \cdot \left(\boldsymbol{I} + \eta_* \, \tilde{\boldsymbol{C}} \right)^{-1} \right) \cdot \tilde{\boldsymbol{F}}^T \\
= \quad & \sum_{i=1}^{3} \tilde{\lambda}_i \vec{n}_i \vec{n}_{0_i} \cdot \left(\sum_{i=1}^{3} \frac{\tilde{\lambda}_i^2}{\left(1 + \eta_* \, \tilde{\lambda}_i^2 \right)^2} \vec{n}_{0_i} \vec{n}_{0_i} \right) \cdot \sum_{i=1}^{3} \tilde{\lambda}_i \vec{n}_{0_i} \vec{n}_i \\
= \quad & \sum_{i=1}^{3} \frac{\tilde{\lambda}_i^4}{\left(1 + \eta_* \, \tilde{\lambda}_i^2 \right)^2} \vec{n}_i \vec{n}_i \\
= \quad & \tilde{\boldsymbol{B}} \cdot \left(\boldsymbol{I} + \eta_* \, \tilde{\boldsymbol{B}} \right)^{-1} \cdot \left(\boldsymbol{I} + \eta_* \, \tilde{\boldsymbol{B}} \right)^{-1} \cdot \tilde{\boldsymbol{B}}.
\end{aligned} \tag{C.36}
$$

Finally, the expression for the Cauchy stress tensor can be completed by substituting Equation C.33 into Equation C.23 and rewriting using the expressions that were just derived:

$$
\boldsymbol{\sigma} = \frac{N_s \, k \, T}{J} \left(\tilde{\boldsymbol{B}} \cdot \boldsymbol{Z} \right)^d, \tag{C.37}
$$

where the tensor $\boldsymbol{Z}$ is introduced:

$$
\begin{aligned}
\boldsymbol{Z} \quad = \quad & \frac{\alpha_*^2 (1 + \eta_*)(1 - \alpha_*^2)}{\left(1 - \alpha_*^2 \, \mathrm{tr} \left(\tilde{\boldsymbol{B}} \right) \right)^2} \, \mathrm{tr} \left(\tilde{\boldsymbol{B}} \cdot \left(\boldsymbol{I} + \eta_* \, \tilde{\boldsymbol{B}} \right)^{-1} \right) \boldsymbol{I} \\
& + \frac{(1 + \eta_*)(1 - \alpha_*^2)}{1 - \alpha_*^2 \, \mathrm{tr} \left(\tilde{\boldsymbol{B}} \right)} \left(\left(\boldsymbol{I} + \eta_* \, \tilde{\boldsymbol{B}} \right)^{-1} - \eta_* \left(\boldsymbol{I} + \eta_* \, \tilde{\boldsymbol{B}} \right)^{-1} \cdot \left(\boldsymbol{I} + \eta_* \, \tilde{\boldsymbol{B}} \right)^{-1} \cdot \tilde{\boldsymbol{B}} \right) \\
& + \eta_* \left(\boldsymbol{I} + \eta_* \, \tilde{\boldsymbol{B}} \right)^{-1} - \frac{\alpha_*^2}{1 - \alpha_*^2 \, \mathrm{tr} \left(\tilde{\boldsymbol{B}} \right)} \boldsymbol{I}.
\end{aligned} \tag{C.38}
$$